



**HAL**  
open science

# Skills and Limitations of the Adiabatic Omega Equation: How Effective Is It to Retrieve Oceanic Vertical Circulation at Mesoscale and Submesoscale?

Alice Pietri, Xavier Capet, Francesco d'Ovidio, Marina Lévy, Julien Le Sommer, Jean-Marc Molines, Hervé Giordani

## ► To cite this version:

Alice Pietri, Xavier Capet, Francesco d'Ovidio, Marina Lévy, Julien Le Sommer, et al.. Skills and Limitations of the Adiabatic Omega Equation: How Effective Is It to Retrieve Oceanic Vertical Circulation at Mesoscale and Submesoscale?. *Journal of Physical Oceanography*, 2021, 51 (3), pp.931-954. 10.1175/jpo-d-20-0052.1 . hal-03096579

**HAL Id: hal-03096579**

**<https://hal.science/hal-03096579v1>**

Submitted on 5 Jan 2021

**HAL** is a multi-disciplinary open access archive for the deposit and dissemination of scientific research documents, whether they are published or not. The documents may come from teaching and research institutions in France or abroad, or from public or private research centers.

L'archive ouverte pluridisciplinaire **HAL**, est destinée au dépôt et à la diffusion de documents scientifiques de niveau recherche, publiés ou non, émanant des établissements d'enseignement et de recherche français ou étrangers, des laboratoires publics ou privés.

1 **Skills and limitations of the adiabatic omega equation: how effective is it to**  
2 **retrieve oceanic vertical circulation at meso and submesoscale ?**

3 Alice Pietri<sup>\*†</sup>, Xavier Capet, Francesco d'Ovidio, Marina Levy

4 *Laboratoire d'Océanographie et du Climat, Institut Pierre Simon Laplace (LOCEAN,*  
5 *CNES/CNRS/IRD/MNHN/SU), Paris, France*

6 Julien Le Sommer, Jean-Marc Molines

7 *Univ. Grenoble-Alpes (CNRS/IRD/IGE), Grenoble, France*

8 Hervé Giordani

9 *Centre National de Recherches, Météorologiques, Météo-France, Toulouse, France*

10 *\*Corresponding author address: Alice Pietri, LOCEAN-IPSL/CNES, Jussieu, Paris.*

11 E-mail: [alice.pietri@locean-ipsl.upmc.fr](mailto:alice.pietri@locean-ipsl.upmc.fr)

12 *†Current affiliation: Instituto del Mar del Peru (IMARPE), Callao, Perú.*

## ABSTRACT

13 The quasi-geostrophic and the generalized omega equations are the most  
14 widely used methods to reconstruct vertical velocity ( $w$ ) from *in-situ* data.  
15 As observational networks with much higher spatial and temporal resolutions  
16 are being designed, the question rises of identifying the approximations and  
17 scales at which an accurate estimation of  $w$  through the omega equation can  
18 be achieved and what are the critical scales and observables needed. In this  
19 paper we test different adiabatic omega reconstructions of  $w$  over several re-  
20 gions representative of main oceanic regimes of the global ocean in a fully  
21 eddy-resolving numerical simulation with a  $1/60^\circ$  horizontal resolution. We  
22 find that the best reconstructions are observed in conditions characterized by  
23 energetic turbulence and/or weak stratification where near-surface frontal pro-  
24 cesses are felt deep into the ocean interior. The quasi-geostrophic omega  
25 equation gives satisfactory results for scales larger than  $\sim 10$  km horizon-  
26 tally while the improvements using a generalized formulation are substantial  
27 only in conditions where frontal turbulent processes are important (provid-  
28 ing improvements with satisfactory reconstruction skill down to  $\sim 5$  km in  
29 scale). The main sources of uncertainties that could be identified are related  
30 to processes responsible for ocean thermal wind imbalance (TWI), which is  
31 particularly difficult to account for (especially in observation-based studies)  
32 and to the deep flow which is generally improperly accounted for in omega  
33 reconstructions through the bottom boundary condition. Nevertheless, the  
34 reconstruction of mesoscale vertical velocities may be sufficient to estimate  
35 vertical fluxes of oceanic properties in many cases of practical interest.

## 36 1. Introduction

37 In geophysical fluids, the combined effect of stratification and rotation strongly inhibits vertical  
38 velocities over a broad range of horizontal scales ( $L_h$ ), near and above the so-called deformation  
39 radius (Rd), typically 30 km in the ocean. Vertical velocities remain small even for  $L_h$  much below  
40 Rd (Pollard and Regier 1992; Giordani et al. 2006), typically a few meters to several tens of me-  
41 ters per day for submesoscale motions,  $L_h \sim O(1)$  km, although their intensity tends to increase  
42 somewhat at finer scales. Much weaker than horizontal advection, vertical transport of oceanic  
43 properties such as heat and biogeochemical tracers is nevertheless of crucial importance for the  
44 overall functioning of the world ocean (Lévy et al. 2012a). In some regions, atmospheric forc-  
45 ings are such that the large-scale flow (100 km and larger) has a vertical component, *e.g.*, under  
46 the influence of coastal upwelling favourable winds or positive wind stress curl. At finer scale  
47 (1-100km) intermittent vertical velocities are associated with the mesoscale and submesoscale tur-  
48 bulence and can be generated by forced and unforced motions such as frontogenesis, baroclinic  
49 instabilities or air-sea interactions, with possible coupling between them (*e.g.* Thomas and Lee  
50 2005). They are responsible for vertical fluxes that have proved difficult to quantify but are widely  
51 believed to play a major role in the heat (Ferrari 2011; Su et al. 2020; Siegelman et al. 2020) and  
52 salt budgets (Lien et al. 2014), in the carbon and nutrient cycles (Ledwell et al. 2008; Balwada  
53 et al. 2018), and in shaping oceanic biodiversity (Lévy et al. 2010, 2012b, 2014, 2018; Siegelman  
54 et al. 2020). It should be noted that vertical velocities also vary at the scales smaller than the  
55 submesoscale in particular vertical fluxes associated with 3D turbulence (Whitt et al. 2019). How-  
56 ever the submesoscale-mesoscale (hereafter SMS) range on which this study focuses is important  
57 because i) it presumably contains a large fraction of co-variance between  $w$  and many key tracer  
58 fields (Ledwell et al. 2008; Chenillat et al. 2015; Balwada et al. 2018), ii) SMS vertical motions

59 can be coherent over relatively long/large time/space scales (including vertically) such that they  
60 produce long range vertical displacements and fluxes, *e.g.*, , organic and inorganic carbon from the  
61 euphotic layer into the dark ocean (Boyd et al. 2019).

62 Direct measurements of vertical velocities with SMS spatiotemporal resolution would thus be  
63 highly desirable. However the magnitude of  $w$  at these scales is typically  $O(1) \text{ mm s}^{-1}$  ( $\sim 100 \text{ m}$   
64  $\text{day}^{-1}$ ) or less (*e.g.*, up to  $2\text{-}3 \text{ mm s}^{-1}$  in the highly turbulent Gulf Stream, Lindstrom and Watts  
65 1994) which places them below the noise level of any existing current meter for the typical time  
66 scales of a few days to weeks over which they vary. Different ingenious ways to circumvent this  
67 difficulty have been developed over time. For instance, direct integrated measurements of vertical  
68 displacements  $\int w dt$  have been made using Lagrangian drifters (Bower and Rossby 1989; D’Asaro  
69 et al. 2004; Steffen and D’Asaro 2002). Alternatively, indirect reconstruction methods have been  
70 proposed based on the heat/density conservation equation (Strass 1994; Lindstrom et al. 1997; Yu  
71 et al. 2019), the vorticity equation (Strass 1994; Giordani et al. 2005) or the 3D non-divergence of  
72 the flow (Helber and Weisberg 2001; Horii et al. 2011). A different framework has also emerged  
73 to infer vertical velocities from the theory of surface quasigeostrophy (SQG) (Held et al. 1995;  
74 Lapeyre and Klein 2006a; LaCasce and Mahadevan 2006), where the 3D flow structure can be  
75 essentially determined from the knowledge of the surface buoyancy field (Isern-Fontanet et al.  
76 2006; Klein et al. 2009; Ponte and Klein 2013; Qiu et al. 2020). Overall, the most commonly used  
77 method to infer  $w$  is based on frontogenetic theories and the so-called omega equation, which is  
78 the subject of the present study.

79 Quasi-geostrophic and semi-geostrophic versions of the omega equation (Hoskins et al. 1978)  
80 have been applied for decades (Leach 1987; Pollard and Regier 1992). The former and to a lesser  
81 extent the latter are by nature suited to low Rossby number environments, *i.e.*, a priori away from  
82 regions of intense vertical velocities. A generalized version of the omega equation was first intro-

83 duced in the atmospheric community (Davies-Jones 1991; Pauley and Nieman 1992; Giordani and  
84 Caniaux 2001) and subsequently applied to the ocean (Viúdez et al. 2002; Giordani et al. 2006).  
85 Vertical velocity forcing processes present in this generalized omega equation are kinetic defor-  
86 mation that arises in shear and confluence situations, mixing and momentum diffusion which can  
87 also disrupt the thermal wind balance and an additional prognostic term due to the rate of change  
88 of unbalanced motions. This latter term shall be zero under the quasi-geostrophic approximation  
89 and is systematically neglected in ocean applications, which makes the omega equation diagnos-  
90 tic for  $w$  (see Qiu et al. 2020 for the only evaluation of this term that we know of). Despite this  
91 simplification, the generalized formulations of the omega equation are expected to hold even in  
92 regions where the flow exhibits high Rossby number (Viúdez et al. 2002; Viúdez and Dritschel  
93 2004; Shearman et al. 2000). Since the omega equation is most frequently used to infer  $w$  from  
94 observations the chosen formulation usually depends on the data available. The adiabatic quasi-  
95 geostrophic version of the equation only requires density observations and a reference level to  
96 derive geostrophic currents from the thermal wind balance. Knowledge of the absolute horizontal  
97 velocity field allows to take into account the effect of the ageostrophic deformation and advection.  
98 Solving more elaborate forms of the omega equation require additional data, such as atmospheric  
99 forcing (Giordani et al. 2006). Statistical methods based on multivariate empirical orthogonal  
100 functions can be used to determine the SMS ocean state from surface satellite information and  
101 sparse in situ data (e.g. ARMOR3D high resolution operational product, Guinehut et al. 2012).  
102 Those methods have been used regularly to infer the forcing terms for omega inversions (Buon-  
103 giorno Nardelli and Santoleri 2005; Buongiorno Nardelli et al. 2012; Buongiorno Nardelli et al.  
104 2018; Barceló-Llull et al. 2018; Buongiorno Nardelli 2020).

105 Numerous investigations of oceanic vertical velocities based on the omega equation have been  
106 carried out since the 1980s, most frequently in the context of mesoscale-resolving observational

107 efforts. A few of them have used independent ways to estimate  $w$  and evaluate the skills of the  
108 omega reconstructions. Conclusions are generally that the omega equation has reasonable skills  
109 at the mesoscale. A few studies have also applied this equation to numerical model outputs to  
110 test its reliability and degree of accuracy (Pinot et al. 1996; Allen et al. 2001; Rixen et al. 2003;  
111 Uchida et al. 2019). The domain of validity and typical errors attached to an omega reconstruction  
112 for realistic cases are however not clearly established. This is particularly true at submesoscale  
113 where the omega equation has been increasingly applied (Pallàs-Sanz et al. 2010). The benefit  
114 that one can expect from using more elaborate versions of the omega equation compared to the  
115 quasigeostrophic formulation are also not clearly established. An overview of the literature on the  
116 subject offers a great diversity of conclusions (from major to no benefits or even degradation of the  
117 reconstruction). We provide a review of omega-reconstructions literature in the the bibliography  
118 table (SI1). Overall, this literature appears to be mainly composed of an accumulation of test cases  
119 (Pascual et al. 2017; Buongiorno Nardelli et al. 2012; Rixen et al. 2003; Allen et al. 2001), many  
120 of which are in idealized settings (Viúdez and Dritschel 2004). These individual cases can be  
121 difficult to compare against one another.

122 The main novelty of the present study is to apply the same analysis framework to assess the skills  
123 of the adiabatic omega equation in several dynamical regimes representative of a broad diversity  
124 of ocean conditions. The aim is to propose a more integrated and comprehensive understanding  
125 of the skills and limitations of omega reconstructions. Given this ambition, we restrict the scope  
126 somewhat by mainly focusing on vertical velocities outside mixed layers, typically at depths  $\sim$   
127 200 – 400 m. Submesoscale velocities in the mixed layer are important too (*e.g.*, Smith et al.  
128 2016) but they more strongly compete and interact with 3D turbulent processes responsible with  
129 intense mixing in ways that are just beginning to be clarified (Thomas and Lee 2005; Hamlington  
130 et al. 2014; Suzuki et al. 2016; Sullivan and McWilliams 2018; Callies and Ferrari 2018). On



131 the other hand, we expect SMS vertical velocities obtained by means of omega reconstruction to  
132 be more readily useful to estimate tracer fluxes below the mixed layer, typically upward fluxes of  
133 nutrient into the euphotic layer (Pascual et al. 2015) or downward fluxes of oxygen into subsurface  
134 hypoxic layers (Thomsen et al. 2016).

135 Exploring the ability of the adiabatic omega equation to reconstruct  $w$  in our realistic, eddy-  
136 resolving, circulation model reveals that, in this depth range, reconstruction skills turn out to be  
137 strongly sensitive to the dynamical regime under consideration, but also to the physical (length)  
138 scale of interest. In particular, it is shown that omega reconstructions perform well for scales  
139 down to  $\sim 10$  km while rapid degradation occurs at smaller scales. Consequently, the best results  
140 are obtained in conditions characterized by high vertical velocity variance which are found in  
141 regions with intense *mesoscale* frontogenesis. On the other hand, relaxing the QG assumptions  
142 with the generalized formulation is shown to have a modest impact on the reconstruction. Instead,  
143 an analysis of the relative importance of the sources of errors reveals that a major impact can  
144 be attributed to the choice of the bottom boundary conditions (BBC). The impact of neglecting  
145 vertical mixing terms, though presently deemed limited to the upper layers, would also require  
146 dedicated investigations.

147 The paper is organized as follows. Data and methods are presented in section 2. In section 4  
148 vertical velocity reconstructions in the different dynamical regimes retained for this study are  
149 evaluated. A series of sensitivities allows us to test the impact of the level of complexity of the  
150 omega equation; the formulation of the discrete problem; and several possible choices related to  
151 the boundary conditions. Some reflections on the sources of errors and the dynamical environment  
152 are offered in the discussion.

## 153 2. Data and Methods

154 Mathematical symbols have their usual meaning.  $T$ ,  $S$ ,  $\rho$  and  $\sigma_t$  refer to (respectively) potential  
155 temperature, salinity, density and potential density anomaly.  $x$  (resp.  $y$  and  $z$ ) and  $u$  (resp.  $v$  and  
156  $w$ ) refer to zonal (resp. meridional and vertical) directions and velocity. More precisely in the case  
157 of vertical velocities we will distinguish true velocities  $w$  from reconstructed velocities denoted  $\omega$   
158 with a subscript that refers to the precise omega equation formulation that is being used (see below  
159 Sec. 2b).  $N^2$  is the buoyancy frequency.

### 160 a. The NATL model

161 The outputs from a submesoscale-permitting numerical simulation are used to reconstruct verti-  
162 cal velocity fields using different versions of the omega equation and compare them to the ground  
163 truth model vertical velocities  $w_{model}$ . The NATL60 MJM155 simulation is run using the NEMO  
164 v3.5 code. It has a horizontal resolution of  $1/60^\circ$  (dx comprised between 0.8 and 1.6 km depend-  
165 ing on the latitude), yielding an effective resolution of  $\sim 10$  dx ( $\sim 10 - 15$  km) (Soufflet et al.  
166 2016). This means that a turbulent feature associated with a typical wavelength around  $\sim 10 - 15$   
167 km (typical scale  $\sim 1.5 - 2$  km) are energetically subjected to a negligible influence of the dissi-  
168 pation operator. Below those scales numerical errors can arise that will affect the representation  
169 of physical processes although the misrepresented dynamics in the model solutions may still share  
170 important properties with the dynamics of the system obtained after resolution convergence (Le  
171 Sommer et al. 2018). On the vertical, the simulation has 300 levels (dz increases with depth  
172 and ranges from 1 to 30 m) and in the range of depths of analysis (200-400 m depth), the ver-  
173 tical resolution is  $\sim 10$  m. The simulation is forced by realistic atmospheric forcings (DFS5.2)  
174 and boundary conditions (GLORYS2V3). It was integrated over a 5 years period (2004-2008)  
175 (Amores et al. 2018; Ducouso et al. 2017; Fresnay et al. 2018).

176 The model domain encompasses the whole North Atlantic. For this study, four contrasted sectors  
177 were selected. For each region, eleven consecutive daily averaged outputs are analysed for two  
178 opposite seasons of the year, in June and December. Near-inertial motions produced by the high-  
179 frequency variability of the atmospheric forcings are partly filtered out and partly aliased in model  
180  $u, v, \sigma_t$  and  $w$  daily fields that are used in this study. A cleaner separation between balanced  
181 and unbalanced motions would be useful to untangle their respective roles (e.g., see Qiu et al.  
182 2020). Lacking the high-frequency model outputs needed to do better, we note that, in most  
183 situations, omega estimations made using observations contain an unknown but presumably larger  
184 inertia-gravity (IG) wave contribution. Our study can thus be considered as a favorable evaluation  
185 in which this source of errors is minimized by the daily averaging. Absence of tidal forcing  
186 in NATL60 will also tend to underestimate the energy level of unbalanced motion (Qiu et al.  
187 2018) and thus has a similar consequence. The relevance of the study to the real ocean context  
188 is however justified by the fact that model vertical velocities in the submesoscale-permitting class  
189 of simulations are known to capture the patterns expected from the theory and observation based  
190 studies.

191 The four regions we focus on are:

192 – the Gulf Stream/LatMix region (Shcherbina et al. 2013, LMX) centered around  $38^\circ\text{N}$  and  
193  $67^\circ\text{W}$ . It encompasses the very energetic Gulf Stream current. It is characterized by intense  
194 mesoscale activity composed of meanders and eddies. Vertical motions in the Gulf Stream  
195 region have been the subject of many studies aimed at describing water exchanges between  
196 the jet core and its vicinities (Bower and Rossby 1989; Lindstrom and Watts 1994; Joyce et al.  
197 2013). This environment and the large amplitude meanders of the Gulf Stream in particular  
198 are well known to produce intense vertical velocities (Fig. 1a).

- 199 – The region of the Azores current (AZO) centered at  $33^{\circ}\text{N}$ ,  $34^{\circ}\text{W}$  which is characteristic of  
200 a subtropical regime with limited atmospheric forcing and modest mesoscale activity. It is  
201 the least energetic of the four regions in terms of vertical velocities (Fig. 1b). We relate this  
202 to the modest role played by surface density contrasts and upper ocean frontogenesis in the  
203 regional dynamics (Lapeyre 2009; Volkov and Fu 2010, 2011)
- 204 – An area of the subpolar gyre South West of Iceland encompassing part of the Rekjanes ridge  
205 (REK) and centered around  $54^{\circ}\text{N}$ ,  $31^{\circ}\text{W}$ . The regional dynamics is characterized by weak  
206 mean flow and a moderately intense mesoscale activity made of deep reaching isolated struc-  
207 tures (Fig. 1c).
- 208 – A sector of the Atlantic North-Eastern margin near  $49^{\circ}\text{N}$  and  $15^{\circ}\text{W}$ , where the Osmosis ex-  
209 periment took place (Buckingham et al. 2016, OSM). The regional dynamics is characterized  
210 by weak large scale circulation, weak mesoscale activity, and a marked seasonality of the  
211 submesoscale activity which is very intense in the wintertime (Fig. 1d; Thompson et al.  
212 2016).

213 To limit the computational cost of inverting the omega equation a 3D sub-domain of each region  
214 is retained with dimensions  $\sim 360$  by  $\sim 270$  km on the horizontal and 1600 m in the vertical (re-  
215 duced depth ranges will also be used in sensitivity tests section 4d). Horizontal (native) resolution  
216 is  $\sim 1.5$  km while the data is linearly interpolated on a regular vertical grid with a 5 m resolution.  
217 For each region, a particular depth is selected to perform some of our analyses. As presented in the  
218 introduction the spirit of this investigation led us to choose depth levels 50 m below the deepest  
219 winter mixed layers encountered in that region so near-surface frontal processes are attenuated at  
220 this depth and our study is useful to make progress on biogeochemical fluxes between the mixed  
221 layer and the ocean interior. Specifically, selected depths of analysis (referred to as  $z_a$ ) are 220 m  
222 for LMX, 250 m for AZO, and 380 m for REK and OSM.

223 *b. Formulations of the omega equation*

224 The underlying principles of the omega equation combine two lines of argument (Hoskins 1982)

225 – kinematical: a turbulent flow stirring an heterogeneous surface buoyancy field produces re-  
226 gions of gradient intensification. Specifically, frontal intensification is promoted in the con-  
227 fluence and shear situations that are frequently encountered in mesoscale turbulent conditions  
228 (e.g. Fig. 2).

229 – dynamical: the thermal wind balance, which should approximately hold at  
230 meso/submesoscale, is disrupted in situations of frontal intensification where density  
231 gradients are enhanced while the vertical velocity shear is being reduced. This leads to the  
232 development of ageostrophic secondary circulations (ASC) that attempt to thwart thermal  
233 imbalance by restoring shear and slumping isopycnals. In the ocean interior this process is very  
234 efficient at preventing frontal intensification which is a further justification for the weakness  
235 of vertical velocities away from the surface. At the air-sea interface, the upper boundary  
236 condition  $w \approx 0$  limits the efficiency of ageostrophic circulations so frontal intensification  
237 can generally proceed further and yield intense vertical velocities.

238 Mathematically, the frontogenesis process is captured by a relationship between the spatial  
239 derivatives of  $w$  and a forcing term expressed as the divergence of a vector of forcings  $\mathbf{Q}$

$$\mathcal{L}(w) = \nabla \cdot \mathbf{Q} \quad (1)$$

240  $\mathcal{L}$  is a second-order differential operator that can also take different forms depending on which  
241 processes responsible for thermal wind disruptions are being considered in  $\mathbf{Q}$ .

242 A starting point to derive the omega equation for the general case is the set of equations govern-  
 243 ing hydrostatic and Boussinesq flows:

$$\frac{du}{dt} - fv = -\frac{1}{\rho_0} \frac{\partial p}{\partial x} + F_x \quad (2)$$

$$\frac{dv}{dt} + fu = -\frac{1}{\rho_0} \frac{\partial p}{\partial y} + F_y \quad (3)$$

$$\frac{d\rho}{dt} = F_\rho \quad (4)$$

$$\nabla \cdot \mathbf{v} = 0 \quad (5)$$

$$(6)$$

244 where  $(F_x, F_y)$  and  $F_\rho$  are source/sink of momentum and buoyancy caused by turbulent mixing.

The flow is then decomposed into a geostrophic ( $\mathbf{v}_g$ ) and ageostrophic ( $\mathbf{v}_{ag}$ ) component

$$\mathbf{v} = \mathbf{v}_g + \mathbf{v}_{ag}$$

245 where the geostrophic velocity satisfies the thermal wind balance:

$$\begin{cases} f \frac{\partial u_g}{\partial z} = \frac{g}{\rho} \frac{\partial \rho}{\partial y} \\ f \frac{\partial v_g}{\partial z} = -\frac{g}{\rho} \frac{\partial \rho}{\partial x} \end{cases} \quad (7)$$

246 and the residual ageostrophic flow component departing from this balance (the so-called thermal  
 247 wind imbalance - TWI) satisfies:

$$\begin{cases} f \frac{\partial u_{ag}}{\partial z} = f \frac{\partial u}{\partial z} - \frac{g}{\rho} \frac{\partial \rho}{\partial y} \\ f \frac{\partial v_{ag}}{\partial z} = f \frac{\partial v}{\partial z} + \frac{g}{\rho} \frac{\partial \rho}{\partial x} \end{cases} \quad (8)$$

248 The generalized omega equation (1) is obtained by manipulating the time evolution equation for  
 249 the TWI and yields (Giordani and Planton 2000):

$$f^2 \frac{\partial^2 w}{\partial z^2} + \nabla_h (N^2 \cdot \nabla_h w) = \nabla \cdot \mathbf{Q}, \quad (9)$$

250 where the  $\mathbf{Q}$  vector involved in the right hand side (rhs) of the equation can be expressed as a sum  
 251 of different forcings:

$$\mathbf{Q} = 2 \underbrace{(\mathbf{Q}_{\text{twg}} + \mathbf{Q}_{\text{twag}})}_{\mathbf{Q}_{\text{tw}}} + \mathbf{Q}_{\text{dag}} + \mathbf{Q}_{\text{dr}} + \mathbf{Q}_{\text{th}} + \mathbf{Q}_{\text{dm}} \quad (10)$$

252 following the notations of Giordani et al. (2006).  $\mathbf{Q}_{\text{tw}}$  is the kinematic deformation and can be de-  
 253 composed into a geostrophic  $\mathbf{Q}_{\text{twg}}$  and an ageostrophic component  $\mathbf{Q}_{\text{twag}}$ .  $\mathbf{Q}_{\text{dag}}$  is the deformation  
 254 of the thermal wind imbalance and  $\mathbf{Q}_{\text{dr}}$  its material rate of change. In all practical situations,  $\mathbf{Q}_{\text{dr}}$   
 255 cannot be estimated and is therefore unaccounted for in the remainder of the study.  $\mathbf{Q}_{\text{th}}$  and  $\mathbf{Q}_{\text{dm}}$   
 256 refer respectively to the diabatic turbulent buoyancy and momentum forcings.

257 Being interested in the ability to determine vertical velocities through and below the thermocline  
 258 we neglect the effects of diffusive momentum and buoyancy fluxes which are mainly active in or  
 259 immediately below the mixed layer (Giordani et al. 2006; Yoshikawa et al. 2012; Thomas et al.  
 260 2010) but have a limited effect on subsurface velocities (Nagai et al. 2006; Yoshikawa et al. 2012).  
 261 In fact, Xie et al. (2017), using microstructure shear measurements to infer the vertical diffusiv-  
 262 ity, derived the vertical mixing terms ( $\mathbf{Q}_{\text{th}}$  and  $\mathbf{Q}_{\text{dm}}$ ) and showed that below the thermocline the  
 263 vertical velocity associated to those terms is one to two order of magnitude smaller than the one  
 264 associated to the deformation of the flow. An exception is the study of (Qiu et al. 2020) in which  
 265 vertical velocities arising from diffusive terms remain of magnitude comparable to those produced  
 266 by ageostrophic deformation ( $\mathbf{Q}_{\text{twag}}$ ) well below the mixed layer. We suspect that this is because  
 267 vertical velocities due to mixing are not calculated explicitly in Qiu et al. (2020) but instead are  
 268 obtained as a residual and thus also contain contributions from various sources such as imperfect  
 269 boundary conditions and other numerical errors (see Sec. 4c and 4d).

270 We will limit ourselves to comparing the two  $\omega$  reconstructions that are most commonly  
 271 used with real ocean data: the QG version where  $\omega_{QG}$  is solely forced by the curvature of the

272 geostrophic flow ( $\mathbf{Q}_{QG} = 2\mathbf{Q}_{tw_g}$ ) as in Hoskins et al. (1978); and a more complete formulation  
 273 (NG) in which the  $\mathbf{Q}$  vector forcing  $\omega_{NG}$  includes some contribution from the ageostrophic flow  
 274 ( $\mathbf{Q}_{NG} = 2\mathbf{Q}_{tw} + \mathbf{Q}_{dag}$ ).

275 The  $\mathbf{Q}_{tw_g}$  vector in the QG formulation has the form:

$$\mathbf{Q}_{tw_g} = \frac{g}{\rho_0} \left( \frac{\partial u_g}{\partial x} \frac{\partial \rho}{\partial x} + \frac{\partial v_g}{\partial x} \frac{\partial \rho}{\partial y}, \frac{\partial v_g}{\partial y} \frac{\partial \rho}{\partial y} + \frac{\partial u_g}{\partial y} \frac{\partial \rho}{\partial x} \right) \quad (11)$$

276 where  $u_g$  and  $v_g$  are the horizontal components of the geostrophic velocity. In this study, these  
 277 velocities are estimated by applying the thermal wind balance downward starting from the sea  
 278 level with the reference velocities at that level being derived from the model sea level anomalies.  
 279 This procedure mimics what can be optimally done with real oceanic data, assuming that sea level  
 280 elevation is known with good accuracy.

281 The NG formulation takes into account the curvature of the total flow and the deformation of the  
 282 ageostrophic flow,

$$\mathbf{Q}_{tw} = \frac{g}{\rho_0} \left( \frac{\partial u}{\partial x} \frac{\partial \rho}{\partial x} + \frac{\partial v}{\partial x} \frac{\partial \rho}{\partial y}, \frac{\partial v}{\partial y} \frac{\partial \rho}{\partial y} + \frac{\partial u}{\partial y} \frac{\partial \rho}{\partial x} \right) \quad (12)$$

$$\mathbf{Q}_{dag} = f \left( \frac{\partial v}{\partial x} \frac{\partial u_{ag}}{\partial z} - \frac{\partial u}{\partial x} \frac{\partial v_{ag}}{\partial z}, \frac{\partial v}{\partial y} \frac{\partial u_{ag}}{\partial z} - \frac{\partial u}{\partial y} \frac{\partial v_{ag}}{\partial z} \right) \quad (13)$$

283 where  $u_{ag}$  and  $v_{ag}$  are the ageostrophic horizontal velocities. In practice,  $u_{ag}$  and  $v_{ag}$  are obtained  
 284 as the difference between model horizontal velocities and the calculated geostrophic velocities  $u_g$   
 285 and  $v_g$ .

286 Two baseline reconstructions  $\omega_{QG}$  and  $\omega_{NG}$  are thus computed from the adiabatic QG and NG  
 287 formulations of the  $\mathbf{Q}$  vector. For each of them the computation is made on the horizontal sub-  
 288 domains defined in section 2a. The domain extension in the vertical goes from the surface down  
 289 to 1600 m. Dirichlet boundary conditions are used at all the frontiers. A tridimensional buoy-  
 290 ancy frequency,  $N^2$ , that varies both in the horizontal and in the vertical is used to solve all the  
 291 inversions, although tests were run using a horizontally averaged profile and little differences were



292 observed (not shown). Specific reconstructions using different resolution, domain size or boundary  
 293 conditions are made to explore sensitivities and described in the corresponding sections.

294 To investigate the relative importance of different sources of errors we will carry out two forms  
 295 of omega reconstruction with either perfect right-hand side ( $\omega$  will be denoted  $\omega_{\dagger}$ ) or perfect  
 296 boundary conditions ( $\omega$  will be denoted  $\omega^*$ ). Perfect rhs omega inversions are computed using  
 297 forcing terms that are derived from model vertical velocities and the lhs of (9):

$$\nabla \cdot \mathbf{Q}_{\dagger} = f^2 \frac{\partial^2 w_{model}}{\partial z^2} + \nabla_h (N^2 \cdot \nabla_h w_{model}). \quad (14)$$

298 Precisely, (14) is evaluated using second order centered differences, i.e. in a way that is consistent  
 299 with how the MUDPACK elliptic solver (Adams 1989) that we use is being implemented. For  
 300 instance, along the x direction we use:

$$\left. \frac{\partial^2 w}{\partial x^2} \right|_i = \frac{1}{\Delta x} \left[ \frac{(w_{i+1} - w_i)}{\Delta x} - \frac{(w_i - w_{i-1})}{\Delta x} \right] \quad (15)$$

301 Alternatively perfect boundary conditions can be imposed by applying  $w_{model}$  at the edges of the  
 302 inversion domain. Note that this is however not precisely possible to do at the ocean surface  
 303 because it is a moving interface in NEMO while it must be held fixed in the solving of the omega  
 304 equation.

### 305 *c. Baroclinic mode decomposition*

306 Under the assumptions of flat bottom and rigid lid at the ocean surface the linearized primitive  
 307 (or quasi-geostrophic) equations governing the horizontal and vertical components of inviscid fluid  
 308 motion can be separated (Cushman-Roisin and Beckers 2011). In the vertical, two sets of normal  
 309 mode eigenfunctions  $F_n$  and  $G_n$  form complete bases onto which pressure/horizontal velocity and  
 310 vertical velocities can respectively be projected (see annex A1).

311 Normal mode decomposition has proved useful even in situations where all above assumptions  
312 are not satisfied and in particular when the bottom of the ocean is not flat (e.g. Rocha et al. 2013).  
313 In order to gain insight into the sources of reconstruction errors normal modes decomposition will  
314 be used to interpret the differences in reconstruction skills for the different regimes.

315 In practice the MODES program available at <http://www.d.umn.edu/~smkelly/software.html>  
316 (Kelly 2016) is used to determine the mode structure at each model point. The modal amplitude  
317 of the model vertical velocity is then determined locally.

### 318 **3. Description of the vertical velocity regimes**

319 The four regions and two seasons selected for this study exhibit contrasted dynamical regimes.  
320 This will allow us to explore the sensitivity of the omega reconstruction behaviour and skills to the  
321 nature of the meso/submesoscale turbulence that produces the vertical velocities. The diversity of  
322 vertical flow behavior is visually illustrated by snapshots of model vertical velocities (Figs. 1, 2,  
323 3, 4, 5) and confirmed by their spectral distribution of variance (Fig. 6a,b).

324 In the LMX region, the displayed vertical section was chosen so as to cross the Gulf Stream  
325 (Fig. 2). In this region the EKE is about ten times higher than in the other regions (Fig. 7c,d),  
326 the root-mean-square (rms) of  $w$  is 3 to 5 times higher (Fig. 7e,f) and intense density fronts are  
327 observed both in June and December (Fig. 2). In the frontal region, the vertical velocity structures  
328 extend down to 1500 m (Fig. 7e,f) depth or more, with peak  $|w|$  in excess of  $80 \text{ m day}^{-1}$ . Overall,  
329 this is the region with the largest vertical velocity variance at all scales and a dominant fraction of  
330 this variance is found at the largest scales fitting in the study domain. Also note that LMX interior  
331 vertical velocities are only weakly affected by the seasonal cycle of the near-surface submesoscale  
332 activity (which is present but hardly visible in Fig. 1).

333 Compared to the LMX region, the AZO region is a lot less energetic (Fig. 7c,d); the isopycns  
334 are flatter; and the horizontal velocities are slower. The vertical circulation is by far the weakest  
335 of all four regions (Fig. 7e, f and 6) and exhibits limited seasonal changes. Vertical velocities are  
336 organized into structures whose size is intermediate (smaller than in LMX but larger than in OSM  
337 and to a lesser extent REK) as readily apparent from the inspection of fields in the physical space  
338 and also from the spectral distribution of  $w$  variance (Fig. 6): in the range of scales larger than 10  
339 km the  $w$  spectrum is flatter (resp. steeper) than that for LMX (resp. REK and OSM).  $w$  patterns  
340 in Fig. 3 also tend to be tilted with respect to the vertical axis. This is a plausible indication that  
341 vertically propagating IG waves are involved in the generation of  $w$  (slanted phase lines associated  
342 with near-inertial waves are found in numerous studies, e.g., Furuichi et al. 2008).

343 In the REK region, the average vertical velocity magnitude is  $O(10 \text{ m day}^{-1})$  with localized  
344 higher values near mesoscale structures that can reach of up to  $100 \text{ m day}^{-1}$  and tend to have a  
345 large vertical extension (Fig. 1 and 4). In the physical space,  $w$  structures are frequently tilted  
346 with respect to the vertical although less so than in AZO. Again this is presumably the signature  
347 of near-inertial wave activity. But contrary to the AZO case, the horizontal patterns visible in  $w$   
348 fields are consistent with the structuring role of the (sub)mesoscale activity particularly during  
349 summer: presence of multipolar  $w$  patterns (Lapeyre and Klein 2006b; Viúdez 2018), that could  
350 be the signature of eddy-induced Ekman pumping and/or vortex Rossby waves (McWilliams et al.  
351 2003; Buongiorno Nardelli 2013; Barceló-Llull et al. 2017), as in the left corner of Fig. 1c; elon-  
352 gated filaments of elevated  $w$  (Capet et al. 2016). During winter the enhancement of mixed layer  
353 submesoscale turbulence is particularly marked (Fig. 1c). Most of the fine-scale  $w$  patterns appear  
354 to be confined into the mixed layer and the visual aspect of the  $w$  field differs noticeably on ei-  
355 ther side of the mixed layer base. On the other hand,  $w$  increases significantly in magnitude from  
356 summer to winter (Fig. 7e,f). In terms of spatial scales summer  $w$  have a clear mesoscale domi-

357 nance with a peak around 50-100 km wavelength. For winter  $w$ , the role of the mesoscale is less  
358 prominent while the contribution associated with submesoscales is strongly reinforced (Fig. 6).

359 Vertical velocities in the OSM region share many similarities with those of REK: magnitude is  
360  $O(10 \text{ m day}^{-1})$ ; flatness of the  $w$  power spectrum in the mesoscale range 50 – 100 km; importance  
361 of the near-surface submesoscales particularly during the wintertime; modest indication of vertical  
362 tilt. The main difference between the two regions is the greater degree of  $w$  continuity across the  
363 mixed layer and upper thermocline in winter, presumably as a consequence of very low upper  
364 ocean stratification in the OSM region (Fig. 7b).

#### 365 **4. Omega reconstruction of the vertical velocity fields**

##### 366 *a. Baseline skill assessment*

367 The skills of the omega reconstructions vary greatly depending on the region and season as illus-  
368 trated qualitatively (resp. as quantified) in Figs. 2-5 (resp. in Fig. 8). Fig. 8 represents the spectral  
369 coherence between the model  $w$  and reconstructed  $\omega$ , i.e., the degree of co-variance between them  
370 as a function of scale. The scales and wavelengths above which the spectral coherence is larger  
371 than 0.6 for the QG and NG inversion are listed in table 1 along with the fraction of  $w$  variance  
372 retained at scales larger than that threshold.

373 In general, omega reconstructions perform best at scales  $\gtrsim 10 - 20$  km. The energetic mesoscale  
374 structures are better reproduced and spectral coherence drops rapidly at scales  $\lesssim 2 - 10$  km, i.e.,  
375 the omega reconstruction are not well-suited in the submesoscale range. This is particularly well  
376 illustrated by the LMX region where spectral coherence reaches levels close to 1 above 20 km scale  
377 but drops below 0.6 around 7 – 8 km (Table 1). On the other hand, there is relatively limited  $w$   
378 variance at fine-scale. Thus, the overall quality of the reconstructions is manifest for the randomly

379 chosen situation shown in Fig. 2 where both the intensity and lateral/vertical extension of the  $w$   
380 poles are well reproduced. Overall, 80 – 90% of the  $w$  signal is captured with a coherence of 0.6  
381 or higher in LMX.

382 Wintertime OSM is a notable exception where coherence levels remain elevated down to 3 km  
383 scales, particularly when ageostrophic effects are accounted for (see below). As in LMX, upper  
384 ocean turbulent stirring and ageostrophic secondary circulations reach down to depths of 300 – 500  
385 m in this region but the deformation radius is much smaller than in LMX and the stratification is  
386 particularly weak. The  $w$  field is thus organised in fine-scale structures that are frequently several  
387 hundred meters thick in the vertical (Fig. 5), many of which are well captured by the omega  
388 reconstruction.

389 In the REK region, the omega equation reproduces adequately some of the stronger and larger  
390 vertical velocity structures organized in alternated bands of upward and downward velocity inten-  
391 sity (Fig. 4). As for the finer slanted structures visible in both seasons but more intense in winter  
392 they are almost completely missed. The spectral coherence peaks for scales of  $\sim 10$  km with lower  
393 coherence for smaller and also larger scales. This might arise because vertical velocities at large  
394 scale are driven by other dynamical processes associated with the terms not retained in our omega  
395 reconstructions such as Ekman and inertial pumping.

396 Finally, in agreement with the visual impression drawn from Fig. 3, omega reconstructions per-  
397 form very poorly for wintertime AZO with spectral coherence systematically below 0.5. Includ-  
398 ing ageostrophic effects has virtually no impact on the reconstruction skill for the AZO region as  
399 clearly illustrated in Fig. 3.

400 More generally, including the ageostrophic terms makes a significant difference for the LMX  
401 and wintertime OSM reconstruction only (the scale where the 0.6 coherence threshold is found  
402 decreases by up to 20% for these cases). We relate this to the fact that high Rossby number

403 dynamics is prevalent in both regions albeit for different reasons. In the LMX sectors, the frontality  
 404 of the Gulf Stream leads to intense turbulent stirring by the mesoscale field. In the OSM sector  
 405 deep mixed layers in winter lead to intense submesoscale activity whose influence reaches to  
 406 great depths owing to the reduced subsurface stratification. Conditions resembling those found for  
 407 winter OSM also exist in the REK region in winter but, in this latter case, the modest stratification  
 408 present around 200 m depth (Fig. 7b) seems sufficient to isolate the interior circulation from the  
 409 influence of the near-surface dynamics and thwart ageostrophic effects, hence the limited increase  
 410 in coherence between  $\omega_{QG}$  and  $\omega_{NG}$  in Fig. 8.

#### 411 *b. Sensitivity to temporal averaging*

412 An important limitation of the omega reconstructions presented in the previous section may  
 413 arise from the role played by IG waves. This role cannot be captured by the forcing terms we  
 414 retained for the expression of  $\mathbf{Q}$  in the QG and NG reconstructions which ignores the material rate  
 415 of change of the thermal wind imbalance ( $\mathbf{Q}_{dr}$  in 10). Using daily averages tends to reduce the  
 416 effects of these processes, particularly where the inertial period is close to 24 h (at  $30^\circ$  latitude),  
 417 but does not eliminate them. It is unclear whether the IG wave and subinertial quasi-balanced  
 418 flow contributions to  $w$  should be separated (see discussion section) but the behavior of the omega  
 419 reconstruction as a function of the temporal scale content of the forcing term  $\nabla \cdot \mathbf{Q}$  is of practi-  
 420 cal as well as theoretical interest. This behavior is explored by increasing the degree of temporal  
 421 averaging that is performed prior to the computation of the omega reconstruction right-hand side.  
 422 All simulated fields are averaged similarly, including  $w_{model}$ . The expectation is that more tem-  
 423 poral averaging will reduce the amount of variance associated with the  $w$  field to be reconstructed  
 424 but improve the skill of the omega reconstruction for that low-passed  $w$ . The existence of such a  
 425 trade-off is confirmed in Fig. 9 for most dynamical regimes. Fig. 9 presents the spectral coherence

426 between  $\omega_{NG}$  and  $w_{model}$  for larger (10 – 25 km) and finer (3 – 10 km) scales as a function of the  
427 remaining variance ratio  $Var(\langle w \rangle_t)/Var(w)$ , where  $\langle \cdot \rangle_t$  is the low-pass temporal averaging  
428 whose length is varied from 1 day (standard output for that study) and 10 days. Results are shown  
429 for  $\omega_{NG}$  but only minor differences were found with  $\omega_{QG}$ .

430 For all regions except LMX an optimum in spectral coherence is found for time-averaging longer  
431 than 1 day, both for the large scales (10 – 25 km) and the fine scales (3 – 10 km). The averaging  
432 period associated with this optimum is between 2 and 5 days. As anticipated, spectral coherence  
433 improvement comes at the expense of a loss of reconstructed  $w$  variance. In several cases the loss  
434 of  $w$  variance is less than 25%: REK, AZO and OSM for the large scales and REK for the fine  
435 scales during summer; OSM for the large scales during winter. Particularly for this latter case the  
436 spectral coherence improvement is substantial and 2-5 day averaging seems justified. Conversely,  
437 the most dramatic improvement in  $(\omega_{NG}, w)$  spectral coherence seen in the AZO region (winter,  
438 10 – 25 km scales, 5-day averaging) has a major effect on the retained  $\omega_{NG}$  variance (only 37% of  
439 the original  $w$  variance) and may be of limited utility in practice.

#### 440 *c. Discretization errors*

441 We also wish to draw the reader’s attention on the delicacies of the omega inversion and the  
442 implications these delicacies have on the estimation of vertical velocities. To do so we attempt to  
443 minimize reconstruction errors. In addition to imposing perfect boundary conditions by applying  
444  $w_{model}$  at the edges of our domain, we also compute a “perfect” right-hand side  $\nabla \cdot \mathbf{Q}_\dagger$  to be used  
445 in the elliptic inversion (see section 2b). The resulting vertical velocity estimate  $\omega_\dagger^*$  found as a  
446 numerical solution is associated with minute errors, on average 3 % with the solving parameter  
447 choices we pass to MUDPACK. These errors result from 1) the imperfect convergence of the  
448 elliptic solver and 2) the imperfect boundary condition at the ocean surface.

449 To gain insight into the sensitivity of the elliptic inversion, variant  $\omega_{\dagger}^*$  were also computed by  
 450 employing a discretization scheme alternative to (15) to calculate  $\nabla_h^2 w_{model}$  in (14):

$$\frac{\partial^2 w}{\partial x^2} \Big|_i = \frac{1}{2\Delta x} \left[ \frac{(w_{i+2} - w_i)}{2\Delta x} - \frac{(w_i - w_{i-2})}{2\Delta x} \right] \quad (16)$$

451 Both schemes are consistent, centered, and second order in accuracy. They only differ by the  
 452 length of their stencil (3 or 5 points).

453 We find that the discretization choice has a moderate but significant impact. In the LMX region  
 454 in June for instance the use of the scheme (16) to compute the ‘‘perfect’’ rhs produces relative  $w$  er-  
 455 rors in excess of 12 %, to be compared with the minimal convergence errors of  $\sim 3$  % with scheme  
 456 (15). The elevated error figure obtained with the second scheme helps place realistic limits to verti-  
 457 cal velocity estimation attempts and draws the attention on the fact that minute errors/uncertainties  
 458 on the rhs of the omega equation can have significant impacts on the reconstructed vertical veloc-  
 459 ities.

#### 460 *d. Sensitivity and errors due to boundary conditions*

461 Finally, an important source of error when solving the omega equation is the choice of the bottom  
 462 boundary condition. As numerous studies have pointed out (Allen and Smeed 1996; Rudnick  
 463 1996; Pascual et al. 2004)  $\omega$  is not very dependant on the lateral boundary conditions but the  
 464 form of the BBC and the depth where it is applied can have a strong impact on the solution of  
 465 the equation (Pidcock et al. 2012; Rudnick 1996). Two types of BBCs are generally used, the  
 466 Dirichlet condition  $w = 0$  or the Neumann condition  $\partial w / \partial z = 0$ . A third one was proposed by  
 467 Rudnick (1996): to limit the influence of the boundary condition on the solution, the vertical grid  
 468 was extended below the depth where observations were available. Over the depth range with no  
 469 observations  $\nabla \cdot \mathbf{Q}$  was simply assumed to be zero. In practice, this led Rudnick (1996) to shift



470 the bottom boundary from 400 m (where the deepest observation was available) to 2524 m depth  
471 where a Dirichlet BBC ( $w = 0$ ) was imposed.

472 To assess the impact of the BBC on the solution we compare the errors obtained for Dirichlet and  
473 Neumann conditions and for different domain extensions, with the bottom boundary depth  $z_{bottom}$   
474 ranging from 150 m to 1600 m (Fig. 10). This is done in the four regions and for the two seasons.  
475 We also test the boundary condition proposed by Rudnick (1996) with two different depths (400  
476 m and 800 m) below which  $\nabla \cdot \mathbf{Q}$  is assumed to be zero down to 800 m and 1600 m respectively.  
477 In this section, the omega reconstruction is solved using  $\nabla \cdot \mathbf{Q}_+$  forcing computed as described in  
478 section 2b so relative errors exceeding a few percents can only be due to boundary conditions.

479 Figure 10 shows the relative errors of omega reconstructions made at the reference depths  $z_a$   
480 when different boundary conditions are applied. The errors at depth  $z_a$  are horizontally and tem-  
481 porally averaged over the entire reconstruction domain on the horizontal and over the 11 consec-  
482 utive daily model outputs. The relative error field can be quite large, generally in excess of 0.5  
483 for domain depths shallower than 500 m, despite a good agreement in  $w$  and  $\omega$  patterns. This is  
484 generally consistent with the findings of several past studies (Pinot et al. 1996; Allen et al. 2001;  
485 Rixen et al. 2003).

486 Relative errors varies with  $z_{bottom}$  in a relatively simple and intuitive way: deeper  $z_{bottom}$  sys-  
487 tematically translates into weaker errors with Neumann or Dirichlet boundary condition. More  
488 precisely, errors tend to stabilize around 20% when  $z_{bottom}$  greater than 1000 – 1500 meters are  
489 used (Table 2), with the notable exception of REK for which relative errors are  $\sim 0.3 - 0.4$  and  
490 still decreasing at  $z_{bottom} = 1600$  m. The most evident manifestation of error saturation behavior  
491 is found for LMX and Neumann boundary conditions, with a threshold around  $z_{bottom} = 700$  m  
492 beyond which little improvement is observed. More generally we note that: the quality of the  
493 reconstruction can vary from low to high depending on the choice being made for the depth of the

494 boundary condition; except in the LMX region the Neumann and Dirichlet boundary conditions  
495 give relatively similar results; the use of a buffer region to increase the domain depth following  
496 Rudnick (1996) can ameliorate the reconstruction skill and provide an optimum over all possible  
497 choices but the improvement is generally marginal. Estimating the relative error as a volume-  
498 average over the whole water volume above the depth where the boundary condition is applied  
499 paints a more complicated picture. For instance, in a number of situations, reconstruction errors  
500 are found to increase when the location of the boundary layer deepens beyond certain thresholds  
501 (not shown). We relate this to the fact that deep vertical velocities can be particularly intense ow-  
502 ing to processes not properly resolved by our implementations of the omega reconstructions (IG  
503 wave activity, flow-topography interaction).

504 In an attempt to gain further insight, we use vertical mode decomposition to characterize the  
505 vertical structure of the  $w$  field. Consider a situation where  $w$  would project onto a single mode,  
506 for instance baroclinic mode 2. In that case,  $w$  systematically vanishes at the zero crossing of  
507  $G_2$  and a Dirichlet boundary condition at that depth would not introduce any error. A perfect  
508 Neumann boundary condition would similarly exist at the zero crossings of  $F_2$ . There are several  
509 potential obstacles preventing this from happening. Most importantly, vertical velocity tends to be  
510 associated with fine horizontal scales and this tends to be also true in the vertical (Fig. 3-5). The  
511 vertical mode decomposition of  $w$  generally involves many modes, and in most cases, less than  
512 half of the  $w$  signal is explained by the sum of the first three vertical modes (Fig. 12, annex A1). It  
513 is therefore impossible to choose a fixed depth where the dominant  $F_n$  or  $G_n$  are zeros. The LMX  
514 regime is an exception where the  $w$  vertical structure projects to a large extent onto the first three  
515 baroclinic modes (Fig. 12). For LMX the smallest reconstruction errors (volume averaged) are  
516 obtained for a Neumann boundary condition placed at approximately 750 m depth (not shown),  
517 *i.e.*, the depth below which errors evaluated at a single depth ( $z_a = 220$  m) tend to reach a plateau

518 around 0.2 – 0.25 (Fig. 10a,e). The 750 m value falls in the depth range where  $F_1$  and  $F_3$  are  
519 very close to zero (Fig. 11a). The link between the vertical mode’s structure and the effect of  
520  $z_{bottom}$  on the reconstruction skill is far less clear for the other three regions. We attribute these  
521 inconsistencies to the limited role played by the gravest baroclinic modes in AZO, REK and OSM  
522 (Fig 12).

523 To better characterize the reconstruction errors due to imperfect (bottom) boundary conditions,  
524 we compute an alternative omega reconstruction  $\omega_{NG}^*$  using perfect  $w_{model}$  information at the  
525 boundaries (see section 2b). Differences between  $\omega_{NG}^*$  and  $w_{model}$ , can only arise from the simpli-  
526 fication made to  $\mathbf{Q}$  in the NG inversion (that is, considering  $\mathbf{Q}_{dr}$ ,  $\mathbf{Q}_{th}$  and  $\mathbf{Q}_{dm}$  as null). They range  
527 from  $\sim 1$  to  $\sim 5$  m day $^{-1}$  depending on the region and season. They are typically one to three times  
528 as high as errors associated with a Dirichlet boundary condition at 1600 m (Table 2) and generally  
529 lower than the ones associated with a Dirichlet boundary condition at 500 m (Fig. 10). Discrepan-  
530 cies in spectral distribution between  $\omega_{NG}^*$  and  $w_{model}$  are much reduced compared to those for  $\omega_{NG}$ .  
531 This is particularly true for the scales below 1 km (Fig. 6c and 6d). A similar skill improvement  
532 is noticeable for the spectral coherence (Fig. 8). A significant fraction of the fine-scale vertical  
533 motions in the upper ocean is thus directly linked to unidentified processes active below 1600 m.  
534 Consistent with previous studies (e.g. see Jouanno et al. 2016) flow-topography interactions is a  
535 likely candidate, which would pose serious difficulties if it were to be explicitly incorporated into  
536 the omega reconstruction approach (inversion would need to be performed for the whole ocean  
537 depth range with the knowledge of the vertical velocity at the ocean floor  $w = -\mathbf{u}\nabla h$ ). We do not  
538 see any prospect for this but this source of errors should be kept in mind.

## 539 5. Discussion

540 Since the 1980s a large number of studies have focused on inferring oceanic vertical velocities  
541 through more or less elaborate forms of the omega equation. Most of them have been applied  
542 to local *in-situ* data, in which the sources of errors are difficult to identify and quantify (see the  
543 bibliography table SI1). In some instances the reconstructed vertical velocity field has been used  
544 to qualitatively interpret concomitant tracer distributions (Pollard and Regier 1992; Rudnick 1996;  
545 Martin and Richards 2001; Allen et al. 2005; Ruiz et al. 2009; Pallàs-Sanz et al. 2010; Rousselet  
546 et al. 2019). The uncertainty on reconstructed  $w$  is an important limitation when doing so (also note  
547 that the vertical tracer distribution at any given time reflects the past history of vertical advection  
548 - and mixing).  $w$  velocities are now increasingly being used quantitatively, e.g., as inputs to tracer  
549 models (Pascual et al. 2015; Barceló-Llull et al. 2016).

550 Model studies have addressed the various sources of errors involved and the ways to reduce their  
551 impact with a general focus on three main issues: i) the merits of more complete versions of the  
552 omega equation; ii) the sensitivity to particular choices of boundary conditions when solving the  
553 omega equation; iii) the errors induced by the lack of resolution, homogeneity, and synopticity of  
554 in situ sampling when the omega reconstruction is applied to real ocean observations (see SI1).  
555 These model-based assessments of  $\omega$  reconstructions were typically performed in simplified flow  
556 conditions, composed of a single coherent eddy or front, with a marked preference for the early  
557 stages of destabilisation of baroclinic zones (Strass 1994; Pinot et al. 1996; Allen et al. 2001;  
558 Rixen et al. 2003; Viúdez 2018). More recently, the omega equation has been used to determine  
559 oceanic vertical velocity fields over larger domains and extended time periods from observation-  
560 based gridded reconstructions of temperature and salinity fields (Pascual et al. 2015; Barceló-Llull  
561 et al. 2016; Buongiorno Nardelli et al. 2018). The resulting  $\omega$  fields can subsequently be used

562 to estimate vertical fluxes and this has been attempted for several biogeochemical tracers, over  
563 different relevant time scales.

564 Overall, a general assessment of the skills and limitations of the omega reconstruction is lacking.  
565 The present study is an effort in that direction that mainly pertains to i) and ii) and we deliberately  
566 excluded errors of the type iii). Although they pose important and perhaps leading-order limi-  
567 tations to  $w$  reconstructions from observations, this type of errors could be significantly reduced  
568 by observing the ocean at higher resolution in specific regions of interest and combining these  
569 observations with fine-scale remotely sensed information and model integrations. Optimal ways  
570 to produce such combinations may involve relocation strategies as proposed in Rixen et al. (2001)  
571 and Pascual et al. (2004). Errors i) and ii) pose different type of challenges that have not received  
572 much attention. We have followed the steps of Strass (1994) whose analyses of the omega re-  
573 construction skills included a scale-dependant coherence diagnostic. An originality of our study  
574 is to estimate the fidelity of  $w$  reconstructions for fully turbulent realistic flows. Several findings  
575 reported in the previous section deserve further discussion.

#### 576 *On the limited skills of omega reconstructions at fine-scale*

577 First, the important limitations to the omega reconstructions found at relatively fine-scale, de-  
578 spite the absence of type iii) errors may seem surprising. Some remarks are thus in order. An  
579 important motivation for this work is the representation of vertical tracer fluxes between the sur-  
580 face and interior of the ocean. Therefore we focused on vertical velocities tens of meters below  
581 the mixed layer. At such depths, vertical velocity spectra are significantly more red than closer  
582 to the surface where whiter spectra have been reported (Ponte and Klein 2013; Klein et al. 2008).  
583 This means that modest levels of variance remain in the scale range where coherence has dropped

584 down. Conversely, a large fraction of  $w$  variance ( $> 60\%$  for all regions and seasons) is found in  
585 the scale range where coherence is above 0.6 (table 1).

586 This being said, the coherence drop off at scales below 10 km is interesting in itself and deserves  
587 further discussion. The only regime for which significant skill is being obtained into submesoscale  
588 range is winter OSM, which clearly stands out in terms of coherence (Fig. 8). This is also the  
589 only regime for which the influence of surface intensified frontal turbulence is found to penetrate  
590 down to the depth of analysis ( $z_a = 380$  m), owing to extremely weak subsurface stratifications.  
591 This regime is also the one for which the NG reconstruction provides the largest improvement  
592 over the QG reconstruction. The lack of reconstruction skills generally found at submesoscale is  
593 therefore not due to a particular difficulty at capturing vertical velocities associated with frontal  
594 turbulence. Instead, we attribute reconstruction errors to the imperfection of the BBC used to  
595 invert the elliptic omega equation and to the neglect of fluctuations in thermal wind imbalance due  
596 to partly or fully unbalanced fast processes such as inertial gravity waves. The former source of  
597 error is identified and quantified explicitly while the importance of the latter is inferred indirectly.  
598 Further elaboration on these two error sources follow.

599 The boundary conditions impact omega reconstructions over the entire study domain owing to  
600 the elliptic nature of the omega equation. It has been known for a long time that the solution can  
601 be improved by properly choosing the type and location of the BBC. We explored the possibility  
602 that the BBC strategies could be rationalised based on vertical mode decompositions. Although  
603 one exception was found in the Gulf Stream region, vertical velocities tend to project onto a large  
604 number of vertical modes (Fig. 12) and no ideal positioning of the BBC can be chosen a priori.  
605 Pushing the BBC position  $z_{bottom}$  toward greater depths leads to reconstruction improvements even  
606 beyond 1500 m. This is not feasible when observations are used to perform omega reconstructions  
607 and the typical choices made in this situation ( $z_{bottom} \sim 500$  m see review table SI1) fall in the range

608 where errors are most sensitive to  $z_{bottom}$ . In the Gulf stream region, vertical velocities associated  
609 with upper ocean frontal dynamics extend deep into the water column and tend to project mainly  
610 onto the first 3 vertical modes (Fig. 12). These properties are qualitatively consistent with the fact  
611 that, for the LMX domain, the Neumann BBC outperforms the Dirichlet BBC and that the relative  
612 error curve as a function of BBC depth levels off for  $z_{bottom}$  below  $\sim 700$  m. Similar behaviors  
613 may presumably be observed in other western boundary regions and the Antarctic Circumpolar  
614 Current region. Finally, note that, given a depth down to which data is available to feed an omega  
615 reconstruction, the so-called telescopic method developed by Rudnick provides at best a marginal  
616 improvement over the classical Dirichlet or Neumann boundary conditions.

617 The presence of inertia-gravity waves near and beyond the drop-off scale is not accounted for  
618 as a source of  $w$  (in our case, neglecting the forcing term  $\mathbf{Q}_{dr}$  was due to limitations on the model  
619 outputs at our disposal but including this term for real ocean situations would pose extremely strin-  
620 gent if not impractical requirements on sampling strategies). The AZO region is the one where  
621 inertia-gravity waves are suspected to play the largest role, if only because balanced turbulence is  
622 very weak there. There may be other more subtle consequences of the inertia-gravity wave activity  
623 on the omega reconstruction we have presented. For instance, REK has more  $w$  variance in winter  
624 but coherence between  $\omega_{NG}$  and  $w_{model}$  is degraded at that season compared to summer. Although  
625 seasonal changes appear comparatively unimportant in the LMX region, a slight coherence degra-  
626 dation occurs in winter: winter coherence for the NG reconstruction is  $\sim 0.1$  lower than in summer  
627 over the scale range 2 – 8 km (gaps are smaller at larger scale but the degradation is noticeable up  
628 to 20 km). Again, signs of enhanced NIW activity for the winter analysis period compared to the  
629 summer one suggest that near-inertial waves are responsible for this degradation.

630 For completeness, two other possible sources of omega reconstruction errors are listed here.  
631 Daily averaged variables are used to compute the forcing terms which are nonlinear combinations

632 of these variables. This means that Reynold-type forcing terms should formally be included due  
633 to rapid (intra-day) fluctuations in  $u$ ,  $v$  and  $\rho$ . Kinetic energy corresponding to motions with tem-  
634 poral scales below 1 day is very low in simulations with  $dx \sim 2$  km and we have assumed that this  
635 is a small effect. It would need to be verified that the same applies when *in-situ* observations are  
636 low-passed filtered prior to computing rhs terms for a real ocean omega reconstruction. Forcing  
637 terms associated with mixing of momentum and buoyancy have also been ignored. This is gen-  
638 erally considered as a valid approximation sufficiently far from the mixed layer while this source  
639 of error is expected to increase at shallower depth (see below for more elaboration on this) in the  
640 context of ocean tracer dynamics. Although generally consistent with our findings the latest results  
641 of Qiu et al. (2020) cast some doubts on the smallness of  $w$ -forcing by buoyancy and momentum  
642 diffusion. In a western boundary context, this term is found to be comparable to  $w$ -forcing by  
643 ageostrophic kinematic deformation and stronger than  $w$ -forcing by thermal wind imbalance de-  
644 formation or thermal wind imbalance tendency, even well into the ocean interior (see their figure  
645 4). This issue would however need to be scrutinized based on an explicit computation of the mixed  
646 effect on  $w$ . Qiu et al. (2020) infer this term as a residual which therefore lumps together various  
647 contributions including that due to BBC errors. Model output limitations have not allowed us to  
648 undertake this.

#### 649 *On the consequences of limited reconstruction skills at fine-scales for tracer dynamics*

650 Ultimately, what matters in most applications is not vertical velocity per se but the vertical  
651 transport of oceanic properties, for instance upward fluxes of dissolved iron enriching the euphotic  
652 layer in the Southern Ocean (Nicholson et al. 2019), or downward fluxes of organic material filling  
653 the ocean interior and having key implications on O<sub>2</sub> consumption and distribution (Boyd et al.  
654 2019). Vertical tracer fluxes arise from vertical motions because upward and downward motions



655 are, on average, associated with distinct tracer values. We find it useful to discuss three types of  
656 limit cases in which this can occur and where the limitations of the omega reconstruction described  
657 above may be more or less problematic depending on the scenario. To this end, we consider a  
658 nutrient-like tracer  $\tau$  whose concentration gradient is directed downward. The same reasoning  
659 would apply to tracer with an upward gradient (e.g., phytoplankton or dissolved oxygen).

660 An important distinction between two types of limit cases can be made depending whether  
661 baroclinic instability (BCI) plays an important role or not.

### 662 Case 1

663 When BCI is important, turbulent vertical motions are strongly constrained by the fact that  
664  $\langle w'b' \rangle > 0$ , where  $b$  refers to buoyancy,  $\langle \cdot \rangle$  is a low-pass averaging operator and the prime notation  
665 refers to deviations from this average. BCI can thus contribute to transport a tracer  $\tau$  vertically  
666 provided that the distributions of  $\tau$  and  $b$  are correlated. Far enough from the surface in the ocean  
667 interior available potential energy (APE) release is mainly achieved through mesoscale velocities  
668 (Lapeyre et al. 2006; Capet et al. 2016). Unless the correlations of  $\tau$  and  $b$  were weak at mesoscale  
669 and strong at submesoscale, the proper description of mesoscale  $w$  would thus suffice to capture  
670 the dominant part of  $\langle w'\tau' \rangle$ . Typically, correlations between a tracer  $\tau$  and buoyancy exist owing  
671 to processes acting at large-scale, although large decorrelation can ensue from biological reactions  
672 (e.g. for oxygen and nitrate). Correlations are then transferred down to smaller scales by turbulent  
673 cascades and decorrelation between buoyancy and  $\tau$  is preferentially found at the finest scales  
674 (see discussion in Fox-Kemper et al. 2013, and references therein). Therefore, we expect omega  
675 reconstructions to be useful in this case despite the limitations we have described.

676 We now turn to the situation where vertical motions are not constrained by baroclinic instabil-  
677 ity and result instead from, e.g., fossil mesoscale/submesoscale turbulence and/or internal wave  
678 activity. In this situation, any water parcel has a well defined reference depth position  $z_{ref}$  (quite

679 independent of horizontal position) around which it may oscillate and an additional process must  
680 be invoked for these oscillations to produce  $\tau$  vertical/diapycnal fluxes. We take a Lagrangian  
681 viewpoint and consider  $\delta z = \int_t w dt$ , the vertical displacement of a water parcel from its equilib-  
682 rium position and we distinguish two limit cases illustrated in Fig. 13.

### 683 Case 2

684 Let us consider the situation in which a sink term for  $\tau$  is located in the euphotic layer where pho-  
685 tosynthesis draws  $\tau$  levels down (Fig. 13 a and b). The  $\tau$  anomalies are schematically represented  
686 for a mesoscale (panel a) and a submesoscale (panel b) upward oscillation where the amplitude  
687 of the oscillations have been chosen so as to reflect the distribution of  $w$  variance found in the  
688 ocean interior for all regimes ( $\delta z^m > \delta z^s$ ). Because  $\delta z^m > \delta z^s$  and also because the mesoscale  
689 excursions last on average longer the photosynthesis sink term for  $\tau$  is more effective at mesoscale  
690 than it is at submesoscale. The tracer biogeochemistry acts as a low-pass filter and a representa-  
691 tion of fine-scale vertical motions is unessential in the determination of tracer vertical fluxes. The  
692 deficiencies of the omega equation evidenced in this study should thus have limited consequences  
693 on the determination of tracer vertical fluxes, e.g., as performed in Barceló-Llull et al. (2016).

694 Note that the depth where the mean gradient of  $\tau$  resides is a parameter that is potentially im-  
695 portant to consider. If this mean gradient were located very close below the mixed layer base,  
696 the region where the photosynthesis sink term is active would be closer and the relative amplitude  
697 of submesoscale vertical motions (compared to that for the mesoscale) would be larger, hence a  
698 stronger influence of submesoscale processes.

### 699 Case 3

700 The last limit case is the one where the only possible modification of the tracer concentration  
701 attached to water parcels is through (vertical/diapycnal) mixing with surrounding water masses  
702 when and where the underlying flow structure produces local shear enhancement. Shear being

703 proportional to spatial derivatives of the velocities, fine-scale vertical motions can potentially have  
704 a major contribution on  $\tau$  vertical/diapycnal fluxes despite their lesser magnitude relative to those  
705 at mesoscale. Reconstructed vertical velocities have a general bias toward overly weak variance  
706 that is particularly pronounced at scales below 30 to 50 km, depending on the regime. This bias  
707 and its impact on the determination of tracer fluxes may be amenable to statistical corrections  
708 if omega reconstructions for case 3 type problems turn out to be of importance. The impact of  
709 (very) fine-scale motions on tracer dynamics is presently accounted for by shear-driven mixing  
710 parametrizations (Gregg 1989; Polzin et al. 1995 and references therein) which represent the ef-  
711 fect of internal gravity wave. There are evidences that different forms of heterogeneities such as  
712 submesoscale flows affect internal wave breaking (Whitt and Thomas 2013; Avicola et al. 2007)  
713 but the utility of the omega equation to incorporate these effects in our ocean representations is  
714 presently unclear.

## 715 **6. Conclusions**

716 The ever expanding coverage of observational networks supplemented by satellite observations  
717 with increasing spatio-temporal resolution like the upcoming SWOT mission (d' Ovidio et al.  
718 2019) was a strong motivation for this work. In the coming years we may be able to estimate  
719 vertical fluxes more accurately and at finer scale than ever before. Today, the most common  
720 tool to infer vertical velocity is the omega equation. In this paper we explored the ability of the  
721 most common configurations adopted to solve this equation to provide information on the vertical  
722 circulation at different horizontal length scales. The main novelty of our work is to have used a  
723 broad variety of regimes which helped unravel the diversity of reasons underlying the errors in  
724 omega reconstructions of  $w$  fields, depending on the regional dynamics.

725 Generally the adiabatic omega reconstruction gives good results for mesoscale vertical circula-  
726 tion, typically for structures with horizontal scales larger than 10 km. These structures tend to be  
727 associated with a large part of the  $w$  variance, although their relative importance and the precise  
728 skills of the omega reconstruction at such scales depend on the local dynamics. Omega reconstruc-  
729 tion skills degrade strongly in the submesoscale range. This degradation is manifest both in terms  
730 of reduced variance levels and lack of coherence when comparing reconstructed and true vertical  
731 velocities. There are two main reasons explaining these findings: the overall weakness of (true)  
732  $w$  variance levels below the surface boundary layer in the submesoscale range; the coexistence in  
733 that range of several processes contributing to vertical motions, not just frontal turbulence but also  
734 inertia-gravity waves which force vertical velocities through terms that are generally not accessi-  
735 ble. Overall, the best reconstructions are thus observed in conditions characterised by energetic  
736 turbulence and/or weak stratification (such that near-surface frontal processes are felt well into  
737 the ocean interior). In particular we observed the best results in regimes for a western boundary  
738 (LMX with elevated EKE) and wintertime Porcupine Abyssal Plain (OMS, very weak water col-  
739 umn stratification). Conversely the weak vertical flow found in the AZO region where EKE is low  
740 and subsurface stratification is relatively strong is poorly captured by the omega approach.

741 Implications on the role of submesoscale vertical velocities and whether/how to integrate them  
742 into our representations of property exchanges in the ocean interior will require further elabora-  
743 tion. Numerous studies have highlighted the strong impact frontal submesoscale turbulence can  
744 have on physical and biogeochemical fluxes (Lapeyre et al. 2006; Klein et al. 2008; Thomas and  
745 Ferrari 2008; Capet et al. 2008). For a given tracer  $\tau$ , this is only true to the extent that the mean  
746 distribution of  $\tau$  exhibits vertical contrasts sufficiently close to the surface where frontal activity  
747 remains important. How close depends on the background environment and in particular on the

748 upper ocean stratification. The Surface Quasi-Geostrophic (SQG) theory is useful to qualitatively  
749 apprehend this dependence (Lapeyre et al. 2006).

750 In most past studies dealing with vertical velocities a quasi geostrophic version of the omega  
751 equation was used, but more recently, several authors have included higher order terms. For this  
752 reason, we also evaluated the possible improvements obtained by using a more elaborate version of  
753 the adiabatic equation compared to the simple quasi geostrophic formulation. NG reconstructions  
754 that include ageostrophic forcing terms due to flow deformation leads to improved reconstructions.  
755 The improvements are substantial only in conditions where near-surface frontal processes (i.e.,  
756 submesoscales) are important. This finding has important implications in the context of efforts  
757 aimed at estimating vertical velocities in the real ocean because the adiabatic QG reconstruction  
758 only requires the knowledge of the density field and of the sea surface height (or a reference level  
759 of no motion).

760 The consequences of various numerical choices on the reconstruction skills have been investi-  
761 gated in this work. Choices made for the bottom boundary condition have a major impact. Pushing  
762 the boundary condition as deep as possible is the only rule of thumb that can be provided. The  
763 relative performance of the Dirichlet versus Neumann boundary conditions cannot be anticipated  
764 a priori while the BBC tweak proposed by Rudnick (1996) offers at best marginal improvements.  
765 Obviously, omega reconstruction skills will worsen when it is applied to real observations with  
766 lesser spatial resolution (for the ocean interior data), synopticity issues and instrumental errors.

767 APPENDIX

768 **A1. Baroclinic mode decomposition**

769 To support the results in section 4d, we use a normal mode decomposition to establish possible  
 770 relations between the depth of the vertical boundary condition and the error committed when  
 771 estimated  $w$  with  $\omega$ . The eigenfunctions are solution of the eigenvalues problem:

$$\frac{\partial^2 G_n}{\partial z^2} + \frac{N^2}{c_n^2} G_n = 0 \quad (\text{A1})$$

772 or

$$\frac{\partial}{\partial z} \left( \frac{1}{N^2} \frac{\partial F_n}{\partial z} \right) + \frac{1}{c_n^2} F_n = 0 \quad (\text{A2})$$

773 with the boundary conditions:

$$G_n = 0 \text{ at } z = 0 \text{ and } z = -H \quad (\text{A3})$$

774

$$\frac{\partial F_n}{\partial z} = 0 \text{ at } z = 0 \text{ and } z = -H \quad (\text{A4})$$

775 where the vertical velocity modes  $G_n$  and the pressure modes  $F_n$  are related through the relation,

$$F_n = \frac{\partial G_n}{\partial z}. \quad (\text{A5})$$

776 Vertical variability can then be projected onto the vertical modes  $F_n$  and  $G_n$  so that,

$$p(x, y, z, t) = \sum_{n=0}^{\infty} \tilde{p}_n(x, y, t) F_n(z) \quad (\text{A6})$$

777

$$w(x, y, z, t) = \sum_{n=0}^{\infty} \tilde{w}_n(x, y, t) G_n(z), \quad (\text{A7})$$

778 with  $\tilde{p}_n$  and  $\tilde{w}_n$  the modal amplitudes of the pressure and vertical velocity respectively.

779 To investigate more thoroughly the contribution of the vertical modes to the vertical velocity  
 780 signal, we expressed the vertical velocity by the projection on the three firsts vertical modes and a  
 781 residue,

$$w(x, y, z, t) = \sum_{n=1}^N \tilde{w}_n(x, y, t) G_n(z) + \varepsilon. \quad (\text{A8})$$

782  $\varepsilon$  was estimated for  $N = [1 : 3]$ . The number of profiles where  $\varepsilon/w$  was lower than 0.5, that is to  
783 say that more than half of the  $w$  dynamics is explained by the first one, two or three vertical modes,  
784 was estimated (Fig. 12).

785 Note that in Figure 11,  $F_n$  and  $G_n$  are calculated for a mean stratification that is obtained using  
786 spatial averaging over the entire region and time averaging over 11 daily model outputs. However  
787 they do not differ substantially from the modes calculated on each point and used to infer modal  
788 amplitudes (Sec. 2c).

789 *Acknowledgments.* This work has been partly supported by the NASA/CNES Tosca project  
790 BIOSWOT. Alice Pietri was supported by a CNES postdoctoral grant. The authors wish to  
791 thanks the SWOT cal/val team for providing an stimulating environment in the development  
792 of our study. The NATL60 simulation can be accessed at [https://meom-group.github.io/swot-](https://meom-group.github.io/swot-natl60/access-data.html)  
793 [natl60/access-data.html](https://meom-group.github.io/swot-natl60/access-data.html). The authors wish to thank two anonymous reviewers for their comments  
794 and suggestions for improving the paper.

## 795 **References**

796 Adams, J. C., 1989: mudpack: Multigrid portable fortran software for the efficient solution of  
797 linear elliptic partial differential equations. *Applied Mathematics and Computation*, **34 (2)**, 113–  
798 146, doi:10.1016/0096-3003(89)90010-6.

799 Allen, J. T., and D. Smeed, 1996: Potential Vorticity and Vertical Velocity at the Iceland-Faeroes  
800 Front. *Journal of Physical Oceanography*, **26**, 2611–2634.

801 Allen, J. T., D. A. Smeed, A. J. G. Nurser, J. W. Zhang, and M. Rixen, 2001: Diagnosis of  
802 vertical velocities with the QG omega equation: A relocation method to obtain pseudo-synoptic

803 data sets. *Deep-Sea Research Part I: Oceanographic Research Papers*, **48 (6)**, 1347–1373, doi:  
804 10.1016/S0967-0637(00)00085-6.

805 Allen, J. T., and Coauthors, 2005: Diatom carbon export enhanced by silicate upwelling in the  
806 northeast Atlantic. *Nature*, **437**, 1–5, doi:10.1038/nature03948.

807 Amores, A., G. Jordà, T. Arsouze, and J. Le Sommer, 2018: Up to What Extent Can We Charac-  
808 terize Ocean Eddies Using Present-Day Gridded Altimetric Products? *Journal of Geophysical*  
809 *Research: Oceans*, **123 (10)**, 7220–7236, doi:10.1029/2018JC014140.

810 Avicola, G. S., J. N. Moum, A. Perlin, and M. D. Levine, 2007: Enhanced turbulence due to  
811 the superposition of internal gravity waves and a coastal upwelling jet. *Journal of Geophysical*  
812 *Research: Oceans*, **112 (6)**, 1–20, doi:10.1029/2006JC003831.

813 Balwada, D., K. S. Smith, and R. Abernathey, 2018: Submesoscale Vertical Velocities Enhance  
814 Tracer Subduction in an Idealized Antarctic Circumpolar Current. *Geophysical Research Let-*  
815 *ters*, **45 (18)**, 9790–9802, doi:10.1029/2018GL079244.

816 Barceló-Llull, B., E. Mason, A. Capet, and A. Pascual, 2016: Impact of vertical and horizontal  
817 advection on nutrient distribution in the southeast Pacific. *Ocean Science*, **12 (4)**, 1003–1011,  
818 doi:10.5194/os-12-1003-2016.

819 Barceló-Llull, B., E. Pallàs-Sanz, P. Sangrà, A. Martínez-Marrero, S. N. Estrada-Allis, and  
820 J. Arístegui, 2017: Ageostrophic Secondary Circulation in a Subtropical Intrathermocline Eddy.  
821 *Journal of Physical Oceanography*, **47 (5)**, 1107–1123, doi:10.1175/jpo-d-16-0235.1.

822 Barceló-Llull, B., A. Pascual, E. Mason, and S. Mulet, 2018: Comparing a Multivariate Global  
823 Ocean State Estimate With High-Resolution in Situ Data: An Anticyclonic Intrathermocline



824 Eddy Near the Canary Islands. *Frontiers in Marine Science*, **5**, 1–15, doi:10.3389/fmars.2018.  
825 00066.

826 Bower, A., and T. Rossby, 1989: Evidence of Cross-Frontal Exchange Processes in the Gulf  
827 Stream Based on Isopycnal RAFOS Float Data. *Journal of Physical Oceanography*, **19**, 1177–  
828 1190.

829 Boyd, P. W., H. Claustre, M. Levy, D. A. Siegel, and T. Weber, 2019: Multi-faceted par-  
830 ticle pumps drive carbon sequestration in the ocean. *Nature*, **568**, 327–335, doi:10.1038/  
831 s41586-019-1098-2.

832 Buckingham, C. E., and Coauthors, 2016: Seasonality of submesoscale flows in the ocean surface  
833 boundary layer. *Geophysical Research Letters*, **43**, 2118–2126.

834 Buongiorno Nardelli, B., 2013: Vortex waves and vertical motion in a mesoscale cyclonic eddy.  
835 *Journal of Geophysical Research: Oceans*, **118** (10), 5609–5624, doi:10.1002/jgrc.20345.

836 Buongiorno Nardelli, B., S. Guinehut, A. Pascual, Y. Drillet, S. Ruiz, and S. Mulet, 2012: Towards  
837 high resolution mapping of 3-d mesoscale dynamics from observations. *Ocean Science*, **8**, 885–  
838 901, doi:10.5194/os-8-885-2012.

839 Buongiorno Nardelli, B., S. Mulet, and D. Iudicone, 2018: Three-Dimensional Ageostrophic Mo-  
840 tion and Water Mass Subduction in the Southern Ocean. *Journal of Geophysical Research:*  
841 *Oceans*, **123** (2), 1533–1562, doi:10.1002/2017JC013316.

842 Buongiorno Nardelli, B., and R. Santoleri, 2005: Methods for the reconstruction of vertical profiles  
843 from surface data: Multivariate analyses, residual GEM, and variable temporal signals in the  
844 North Pacific Ocean. *Journal of Atmospheric and Oceanic Technology*, **22** (11), 1762–1781,  
845 doi:10.1175/JTECH1792.1.

846 Buongiorno Nardelli, B., 2020: A multi-year time series of observation-based 3D horizontal and  
847 vertical quasi-geostrophic global ocean currents. *Earth System Science Data*, **12**(3), 1711–1723,  
848 doi:10.5194/essd-12-1711-2020.

849 Callies, J., and R. Ferrari, 2018: Baroclinic instability in the presence of convection. *Journal of*  
850 *Physical Oceanography*, **48**, 45–60.

851 Capet, X., P. Klein, B. L. Hua, G. Lapeyre, and J. C. McWilliams, 2008: Surface kinetic energy  
852 transfer in surface quasi-geostrophic flows. *Journal of Fluid Mechanics*, **604**, 165–174, doi:  
853 10.1017/S0022112008001110.

854 Capet, X., G. Roullet, P. Klein, and G. Maze, 2016: Intensification of Upper-Ocean Submesoscale  
855 Turbulence through Charney Baroclinic Instability. *Journal of Physical Oceanography*, **46** (11),  
856 3365–3384, doi:10.1175/jpo-d-16-0050.1.

857 Chenillat, F., B. Blanke, N. Grima, P. J. S. Franks, X. Capet, and P. Rivière, 2015: Quantify-  
858 ing tracer dynamics in moving fluids: a combined Eulerian-Lagrangian approach. *Frontiers in*  
859 *Environmental Science*, **3** (June), 1–15, doi:10.3389/fenvs.2015.00043.

860 Cushman-Roisin, B., and J.-M. Beckers, 2011: *Introduction to Geophysical Fluid Dynamics*, Vol.  
861 101. 2nd ed., Academic Press, 875 pp.

862 d’Ovidio, F., and Coauthors, 2019: Frontiers in fine-scale in situ studies: Opportunities during  
863 the SWOT fast sampling phase. *Frontiers in Marine Science*, **6**, doi:10.3389/fmars.2019.00168.

864 D’Asaro, E. A., K. B. Winters, and R. C. Lien, 2004: Lagrangian estimates of diapycnal mixing in  
865 a simulated K-H instability. *Journal of Atmospheric and Oceanic Technology*, **21** (5), 799–809,  
866 doi:10.1175/1520-0426(2004)021<0799:LEODMI>2.0.CO;2.

867 Davies-Jones, R., 1991: The frontogenetical forcing of secondary circulations. part i: The duality  
868 and generalization of the q vector. *Journal of the Atmospheric Sciences*, **48 (4)**, 497–509, doi:  
869 10.1175/1520-0469(1991)048<0497:TFFOSC>2.0.CO;2.

870 Ducouso, N., J. Le Sommer, J. M. Molines, and M. Bell, 2017: Impact of the Symmetric Instabil-  
871 ity of the Computational Kind at mesoscale- and submesoscale-permitting resolutions. *Ocean*  
872 *Modelling*, **120 (October)**, 18–26, doi:10.1016/j.ocemod.2017.10.006.

873 Ferrari, R., 2011: A frontal challenge for climate models. *Science*, **332 (6027)**, 316–317, doi:  
874 10.1126/science.1203632.

875 Fox-Kemper, B., R. Lumpkin, and F. O. Bryan, 2013: Lateral transport in the ocean interior. *Ocean*  
876 *Circulation and Climate: A 21st century perspective*, G. Siedler, S. M. Griffies, J. Gould, and  
877 J. A. Church, Eds., Academic Press (Elsevier Online), International Geophysics, Vol. 103, 185–  
878 209.

879 Fresnay, S., A. L. Ponte, S. Le Gentil, and J. Le Sommer, 2018: Reconstruction of the 3-D Dy-  
880 namics From Surface Variables in a High-Resolution Simulation of North Atlantic. *Journal of*  
881 *Geophysical Research: Oceans*, **123 (3)**, 1612–1630, doi:10.1002/2017JC013400.

882 Furuichi, N., T. Hibiya, and Y. Niwa, 2008: Model-predicted distribution of wind-induced internal  
883 wave energy in the world’s oceans. *Journal of Geophysical Research: Oceans*, **113 (9)**, 1–13,  
884 doi:10.1029/2008JC004768.

885 Giordani, H., and G. Caniaux, 2001: Sensitivity of cyclogenesis to sea surface temperature  
886 in the Northwestern Atlantic. *Monthly Weather Review*, **129 (6)**, 1273–1295, doi:10.1175/  
887 1520-0493(2001)129<1273:SOCTSS>2.0.CO;2.

- 888 Giordani, H., G. Caniaux, and L. Prieur, 2005: A simplified 3D oceanic model assimilating  
889 geostrophic currents: Application to the POMME experiment. *Journal of Physical Oceanog-*  
890 *raphy*, **35** (5), 628–644, doi:10.1175/JPO2724.1.
- 891 Giordani, H., and S. Planton, 2000: Modeling and Analysis of Ageostrophic Circulation over the  
892 Azores Oceanic Front during the SEMAPHORE Experiment. *Monthly Weather Review*, **128** (7),  
893 2270–2287, doi:10.1175/1520-0493(2000)128<2270:maoac>2.0.co;2.
- 894 Giordani, H., L. Prieur, and G. Caniaux, 2006: Advanced insights into sources of vertical velocity  
895 in the ocean. *Ocean Dynamics*, **56** (5-6), 513–524, doi:10.1007/s10236-005-0050-1.
- 896 Gregg, M. C., 1989: Scaling turbulent dissipation in the thermocline. *Journal of Geophysical*  
897 *Research*, **94** (C7), 9686–9698, doi:10.1029/jc094ic07p09686.
- 898 Guinehut, S., A. L. Dhomps, G. Larnicol, and P. Y. Le Traon 2012: High resolution 3-D tem-  
899 perature and salinity fields derived from in situ and satellite observations. *Ocean Science*, **8**(5),  
900 845–857, doi:10.5194/os-8-845-2012.
- 901 Hamlington, P. E., L. P. Van Roekel, B. Fox-Kemper, K. Julien, and G. P. Chini, 2014: Langmuir–  
902 submesoscale interactions: Descriptive analysis of multiscale frontal spindown simulations.  
903 *Journal of Physical Oceanography*, **44**, 2249–2272.
- 904 Helber, R. W., and R. H. Weisberg, 2001: Equatorial upwelling in the western pacific warm pool.  
905 *Journal of Geophysical Research*, **106**, 8989–9003.
- 906 Held, I. M., R. T. Pierrehumbert, S. T. Garner, and K. L. Swanson, 1995: Surface quasi-geostrophic  
907 dynamics. *J. Fluid Mech.*, **282**, 1–20, doi:10.1017/S0022112095000012.

908 Horii, T., Y. Masumoto, I. Ueki, S. P. Kumar, and K. Mizuno, 2011: Intraseasonal vertical ve-  
909 locity variation caused by the equatorial wave in the central equatorial indian ocean. *Journal of*  
910 *Geophysical Research*, **116**.

911 Hoskins, B. J., 1982: the Mathematical theory of frontogenesis. *Ann. Rev. Fluid Mech*, **15 (12)**,  
912 131–151.

913 Hoskins, B. J., I. Draghici, and H. C. Davies, 1978: A new look at the  $\omega$  equation. *Quarterly*  
914 *Journal of the Royal Meteorological Society*, **104 (439)**, 31–38, doi:10.1002/qj.49710443903.

915 Isern-Fontanet, J., B. Chapron, G. Lapeyre, and P. Klein, 2006: Potential use of microwave sea sur-  
916 face temperatures for the estimation of ocean currents. *Geophysical Research Letters*, **33 (24)**,  
917 1–5, doi:10.1029/2006GL027801.

918 Jouanno, J., X. Capet, G. Madec, G. Roullet, and P. Klein, 2016: Dissipation of the energy im-  
919 parted by mid-latitude storms in the Southern Ocean. *Ocean Science*, **12 (3)**, 743–769, doi:  
920 10.5194/os-12-743-2016.

921 Joyce, T. M., J. M. Toole, P. Klein, and L. N. Thomas, 2013: A near-inertial mode observed within  
922 a Gulf Stream warm-core ring. *Journal of Geophysical Research: Oceans*, **118 (4)**, 1797–1806,  
923 doi:10.1002/jgrc.20141.

924 Kelly, S. M., 2016: The Vertical Mode Decomposition of Surface and Internal Tides in the Pres-  
925 ence of a Free Surface and Arbitrary Topography. *Journal of Physical Oceanography*, **46 (12)**,  
926 3777–3788, doi:10.1175/jpo-d-16-0131.1.

927 Klein, P., B. L. Hua, G. Lapeyre, X. Capet, S. Le Gentil, and H. Sasaki, 2008: Upper Ocean  
928 Turbulence from High-Resolution 3D Simulations. *Journal of Physical Oceanography*, **38 (8)**,  
929 1748–1763, doi:10.1175/2007jpo3773.1.

930 Klein, P., J. Isern-Fontanet, G. Lapeyre, G. Roullet, E. Danioux, B. Chapron, S. Le Gentil, and  
931 H. Sasaki, 2009: Diagnosis of vertical velocities in the upper ocean from high resolution sea  
932 surface height. *Geophysical Research Letters*, **36 (12)**, 1–5, doi:10.1029/2009gl038359.

933 LaCasce, J. H., and A. Mahadevan, 2006: Estimating subsurface horizontal and vertical veloc-  
934 ities from sea-surface temperature. *Journal of Marine Research*, **64**, 695–721, doi:10.1357/  
935 002224006779367267.

936 Lapeyre, G., 2009: What Vertical Mode Does the Altimeter Reflect? On the Decomposition in  
937 Baroclinic Modes and on a Surface-Trapped Mode. *Journal of Physical Oceanography*, **39 (11)**,  
938 2857–2874, doi:10.1175/2009jpo3968.1.

939 Lapeyre, G., and P. Klein, 2006a: Dynamics of the Upper Oceanic Layers in Terms of Surface  
940 Quasigeostrophy Theory. *Journal of Physical Oceanography*, **36 (2)**, 165–176, doi:10.1175/  
941 jpo2840.1.

942 Lapeyre, G., and P. Klein, 2006b: Impact of the small-scale elongated filaments on the oceanic ver-  
943 tical pump. *Journal of Marine Research*, **64 (6)**, 835–851, doi:10.1357/002224006779698369.

944 Lapeyre, G., P. Klein, and B. L. Hua, 2006: Oceanic Restratification Forced by Surface Frontoge-  
945 nesis. *Journal of Physical Oceanography*, **36 (8)**, 1577–1590, doi:10.1175/jpo2923.1.

946 Le Sommer, J., E. P. Chassignet, and A. J. Wallcraft, 2018: Ocean Circulation Modeling for Op-  
947 erational Oceanography: Current Status and Future Challenges. *New Frontiers in Operational*  
948 *Oceanography*, E. Chassignet, A. Pascual, J. Tintoré, and J. Verron, Eds., GODAE OceanView,  
949 289–306, doi:10.17125/gov2018.ch12.

950 Leach, H., 1987: The diagnosis of synoptic-scale vertical motion in the seasonal thermocline.  
951 *Deep Sea Research Part A, Oceanographic Research Papers*, **34 (12)**, 2005–2017, doi:10.1016/  
952 0198-0149(87)90095-1.

953 Ledwell, J. R., D. J. McGillicuddy, and L. A. Anderson, 2008: Nutrient flux into an intense  
954 deep chlorophyll layer in a mode-water eddy. *Deep-Sea Research Part II: Topical Studies in*  
955 *Oceanography*, **55 (10-13)**, 1139–1160, doi:10.1016/j.dsr2.2008.02.005.

956 Lévy, M., R. Ferrari, P. J. Franks, A. P. Martin, and P. Rivière, 2012a: Bringing physics to life at  
957 the submesoscale. *Geophysical Research Letters*, **39 (14)**, 1–14, doi:10.1029/2012GL052756.

958 Lévy, M., P. J. Franks, and K. S. Smith, 2018: The role of submesoscale currents in structuring  
959 marine ecosystems. *Nature communications*, **9 (1)**, 4758, doi:10.1038/s41467-018-07059-3.

960 Lévy, M., O. Jahn, S. Dutkiewicz, and M. J. Follows, 2014: Phytoplankton diversity and commu-  
961 nity structure affected by oceanic dispersal and mesoscale turbulence. *Limnology and Oceanog-*  
962 *raphy: Fluids and Environments*, **4 (1)**, 67–84, doi:10.1215/21573689-2768549.

963 Lévy, M., P. Klein, A. Tréguier, D. Iovino, G. Madec, S. Masson, and K. Takahashi, 2010: Mod-  
964 ifications of gyre circulation by sub-mesoscale physics. *Ocean Modelling*, **34 (1-2)**, 1–15, doi:  
965 10.1016/j.ocemod.2010.04.001.

966 Lévy, M., L. Resplandy, P. Klein, G. Madec, A.-M. Trguier, S. Masson, and K. Takahashi, 2012b:  
967 Large-scale impacts of submesoscale dynamics on phytoplankton: Local and remote effects.  
968 *Ocean Modelling*. *Ocean Modelling*, **43-44**, 77–93, doi:10.1016/j.ocemod.2011.12.003.

969 Lien, R.-C., and Coauthors, 2014: The LatMix Summer Campaign: Submesoscale Stirring in  
970 the Upper Ocean. *Bulletin of the American Meteorological Society*, **96 (8)**, 1257–1279, doi:  
971 10.1175/bams-d-14-00015.1.

- 972 Lindstrom, S. S., X. Qian, and D. R. Watts, 1997: Vertical motion in the gulf stream and its relation  
973 to meanders. *Journal of Geophysical Research: Oceans*, **102**, 8485–8503.
- 974 Lindstrom, S. S., and R. D. Watts, 1994: Vertical motion in the gulf stream near 68 w. *Journal of*  
975 *Physical Oceanography*, **24**, 2321–2333.
- 976 Martin, A. P., and K. J. Richards, 2001: Mechanisms for vertical nutrient transport within a North  
977 Atlantic mesoscale eddy. *Deep-Sea Research Part II: Topical Studies in Oceanography*, **48 (4-**  
978 **5)**, 757–773, doi:10.1016/S0967-0645(00)00096-5.
- 979 McWilliams, J. C., L. P. Graves, and M. T. Montgomery, 2003: A formal theory for vortex rossby-  
980 waves and vortex evolution. *Geophysical & Astrophysical Fluid Dynamics*, **97**, 275–309, doi:  
981 10.1080/0309192031000108698.
- 982 Nagai, T., A. Tandon, and D. L. Rudnick, 2006: Two-dimensional ageostrophic secondary circula-  
983 tion at ocean fronts due to vertical mixing and large-scale deformation. *Journal of Geophysical*  
984 *Research: Oceans*, **111 (9)**, 1–18, doi:10.1029/2005JC002964.
- 985 Nicholson, S. A., M. Lévy, J. Jouanno, X. Capet, S. Swart, and P. M. Monteiro, 2019: Iron Supply  
986 Pathways Between the Surface and Subsurface Waters of the Southern Ocean: From Winter  
987 Entrainment to Summer Storms. *Geophysical Research Letters*, **46 (24)**, 14 567–14 575.
- 988 Pallàs-Sanz, E., T. M. Johnston, and D. L. Rudnick, 2010: Frontal dynamics in a California Cur-  
989 rent System shallow front: 2. Mesoscale vertical velocity. *Journal of Geophysical Research:*  
990 *Oceans*, **115 (12)**, C12 068, doi:10.1029/2010JC006474.
- 991 Pascual, A., D. Gomis, R. L. Haney, and S. Ruiz, 2004: A Quasigeostrophic Analysis of a Mean-  
992 der in the Palamós Canyon: Vertical Velocity, Geopotential Tendency, and a Relocation Tech-



993 nique. *Journal of Physical Oceanography*, **34** (10), 2274–2287, doi:10.1175/1520-0485(2004)  
994 034<2274:aqaoam>2.0.co;2.

995 Pascual, A., S. Ruiz, B. Buongiorno Nardelli, S. Guinehut, D. Iudicone, and J. Tintoré, 2015:  
996 Net primary production in the Gulf Stream sustained by quasi-geostrophic vertical exchanges.  
997 *Geophysical Research Letters*, **42** (2), 441–449, doi:10.1002/2014GL062569.

998 Pascual, A., and Coauthors, 2017: A multiplatform experiment to unravel meso- and submesoscale  
999 processes in an intense front (alborex). *Frontiers in Marine Science*, **4**, doi:10.3389/fmars.2017.  
1000 00039.

1001 Pauley, P. M., and S. J. Nieman, 1992: A comparison of quasigeostrophic and nonquasi-  
1002 geostrophic vertical motions for a model-simulated rapidly intensifying marine extratropical cy-  
1003 clone. *Monthly Weather Review*, **120** (7), 1108–1134, doi:10.1175/1520-0493(1992)120<1108:  
1004 ACOQAN>2.0.CO;2.

1005 Pidcock, R., A. Martin, J. Allen, S. C. Painter, and D. Smeed, 2012: The spatial variability of  
1006 vertical velocity in an Iceland basin eddy dipole. *Deep Sea Research Part I: Oceanographic*  
1007 *Research Papers*, **72**, 121–140, doi:10.1016/j.dsr.2012.10.008.

1008 Pinot, J.-M., J. Tintoré, and D.-P. Wang, 1996: A study of the omega equation for diagnosing  
1009 vertical motions at ocean fronts. *Journal of Marine Research*, **54** (2), 239–259, doi:10.1357/  
1010 0022240963213358.

1011 Pollard, R. T., and L. A. Regier, 1992: Vorticity and Vertical Circulation at an Ocean Front.  
1012 *Journal of Physical Oceanography*, **22** (6), 609–625, doi:10.1175/1520-0485(1992)022<0609:  
1013 vavcaa>2.0.co;2.

- 1014 Polzin, K. L., J. M. Toole, and R. W. Schmitt, 1995: Finescale parameterizations of turbulent  
1015 dissipation. *Journal of Physical Oceanography*, **25** (3), 306–328, doi:10.1175/1520-0485(1995)  
1016 025<0306:FPOTD>2.0.CO;2.
- 1017 Ponte, A. L., and P. Klein, 2013: Reconstruction of the upper ocean 3D dynamics  
1018 from high-resolution sea surface height. *Ocean Dynamics*, **63** (7), 777–791, doi:10.1007/  
1019 s10236-013-0611-7.
- 1020 Qiu, B., S. Chen, P. Klein, H. Torres, J. Wang, L. L. Fu, and D. Menemenlis, 2020: Reconstructing  
1021 upper ocean vertical velocity field from sea surface height in the presence of unbalanced motion.  
1022 *Journal of Physical Oceanography*, **49** (10), 55–79, doi:10.1175/JPO-D-19-0172.1.
- 1023 Qiu, B., S. Chen, P. Klein, J. Wang, H. Torres, L.-L. Fu, and D. Menemenlis, 2018: Seasonality in  
1024 transition scale from balanced to unbalanced motions in the world ocean. *Journal of Physical*  
1025 *Oceanography*, **48**, 591–605, doi:10.1175/JPO-D-17-0169.1.
- 1026 Rixen, M., J. T. Allen, R. T. Pollard, and J.-M. Beckers, 2003: Along or across front ocean sur-  
1027 vey strategy? The estimation of quasi-geostrophic vertical velocities and temperature fluxes.  
1028 *Geophysical Research Letters*, **30** (5), n/a–n/a, doi:10.1029/2002gl015810.
- 1029 Rixen, M., J. Beckers, and J. T. Allen, 2001: Diagnosis of vertical velocities with the QG Omega  
1030 equation : a relocation method to obtain pseudo-synoptic data sets. *Deep Sea Research Part I:  
1031 Oceanographic Research Papers*, **48**, 1347–1373.
- 1032 Rocha, C. B., A. Tandon, I. C. Da Silveira, and J. A. M. Lima, 2013: Traditional quasi-geostrophic  
1033 modes and surface quasi-geostrophic solutions in the Southwestern Atlantic. *Journal of Geo-  
1034 physical Research: Oceans*, **118** (5), 2734–2745, doi:10.1002/jgrc.20214.

- 1035 Rousselet, L., and Coauthors, 2019: Vertical Motions and Their Effects on a Biogeochemical  
1036 Tracer in a Cyclonic Structure Finely Observed in the Ligurian Sea. *Journal of Geophysical*  
1037 *Research: Oceans*, 1–14, doi:10.1029/2018JC014392.
- 1038 Rudnick, D. L., 1996: Inferring the geostrophic and vertical velocity fields. *J. of Geophys. Res.*,  
1039 **101 (C7)**, 16,216–291,303.
- 1040 Ruiz, S., A. Pascual, B. Garau, I. Pujol, and J. Tintoré, 2009: Vertical motion in the up-  
1041 per ocean from glider and altimetry data. *Geophysical Research Letters*, **36 (14)**, 1–6, doi:  
1042 10.1029/2009GL038569.
- 1043 Shcherbina, A. Y., E. A. D’Asaro, C. M. Lee, J. M. Klymak, M. J. Molemaker, and J. C.  
1044 McWilliams, 2013: Statistics of vertical vorticity, divergence, and strain in a developed sub-  
1045 mesoscale turbulence field. *Geophysical Research Letters*, **40**, 4706–4711.
- 1046 Shearman, R. K., J. A. Barth, J. S. Allen, and R. L. Haney, 2000: Diagnosis of the three-  
1047 dimensional circulation in mesoscale features with large rossby number. *Journal of Physi-*  
1048 *cal Oceanography*, **30 (11)**, 2687–2709, doi:10.1175/1520-0485(2001)031<2687:DOTTDC>2.  
1049 0.CO;2.
- 1050 Siegelman, L., P. Klein, P. Riviere, A. F. Thompson, H. S. Torres, M. Flexas, and D. Menemenlis  
1051 2020: Enhanced upward heat transport at deep submesoscale ocean fronts. *Nature Geoscience*,  
1052 **13**, 50–55, doi:10.1038/s41561-019-0489-1.
- 1053 Smith, K. M., P. E. Hamlington, and B. Fox-Kemper, 2016: Effects of submesoscale turbulence  
1054 on ocean tracers. *Journal of Geophysical Research: Oceans*, **121**, 908–933.

- 1055 Soufflet, Y., P. Marchesiello, F. Lemarié, J. Jouanno, X. Capet, L. Debreu, and R. Benshila, 2016:  
1056 On effective resolution in ocean models. *Ocean Modelling*, **98**, 36–50, doi:10.1016/j.ocemod.  
1057 2015.12.004.
- 1058 Steffen, E. L., and E. A. D’Asaro, 2002: Deep Convection in the Labrador Sea as Observed  
1059 by Lagrangian Floats. *Journal of Physical Oceanography*, **32** (2), 475–492, doi:10.1175/  
1060 1520-0485(2002)032<0475:dcitls>2.0.co;2.
- 1061 Strass, V. H., 1994: Mesoscale Instability and Upwelling. Part 2: Testing the Diagnostics of Verti-  
1062 cal Motion with a Three-Dimensional Ocean Front Model. *Journal of Physical Oceanography*,  
1063 **24** (8), 1759–1767, doi:10.1175/1520-0485(1994)024<1759:miaupt>2.0.co;2.
- 1064 Su, Z., H. S. Torres, P. Klein, A. F. Thompson, L. Siegelman, J. Wang, D. Menemenlis, and  
1065 C. Hill, 2020: High-Frequency Submesoscale Motions Enhance the Upward Vertical Heat  
1066 Transport in the Global Ocean. *Journal of Geophysical Research: Oceans*, **9**, 1–13, doi:  
1067 10.1029/2020JC016544.
- 1068 Sullivan, P. P., and J. C. McWilliams, 2018: Frontogenesis and frontal arrest of a dense filament in  
1069 the oceanic surface boundary layer. *Journal of Fluid Mechanics*, **837**, 341–380.
- 1070 Suzuki, N., B. Fox-Kemper, P. E. Hamlington, and L. P. Van Roekel, 2016: Surface waves affect  
1071 frontogenesis. *Journal of Geophysical Research: Oceans*, **121**, 3597–3624.
- 1072 Thomas, L., and R. Ferrari, 2008: Friction, Frontogenesis, and the Stratification of the Sur-  
1073 face Mixed Layer. *Journal of Physical Oceanography*, **38** (11), 2501–2518, doi:10.1175/  
1074 2008jpo3797.1.
- 1075 Thomas, L. N., and C. M. Lee, 2005: Intensification of Ocean Fronts by Down-Front Winds.  
1076 *Journal of Physical Oceanography*, **35** (6), 1086–1102, doi:10.1175/jpo2737.1.

- 1077 Thomas, L. N., C. M. Lee, and Y. Yoshikawa, 2010: The Subpolar Front of the Japan/East Sea.  
1078 Part II: Inverse Method for Determining the Frontal Vertical Circulation. *Journal of Physical*  
1079 *Oceanography*, **40** (1), 3–25, doi:10.1175/2009jpo4018.1.
- 1080 Thompson, A. F., A. Lazar, C. Buckingham, A. C. Naveira Garabato, G. M. Damerell, and K. J.  
1081 Heywood, 2016: Open-Ocean Submesoscale Motions: A Full Seasonal Cycle of Mixed Layer  
1082 Instabilities from Gliders. *Journal of Physical Oceanography*, **46** (4), 1285–1307, doi:10.1175/  
1083 JPO-D-15-0170.1.
- 1084 Thomsen, S., T. Kanzow, F. Colas, V. Echevin, G. Krahnemann, and A. Engel, 2016: Do subme-  
1085 soscale frontal processes ventilate the oxygen minimum zone off Peru? *Geophysical Research*  
1086 *Letters*, **43** (15), 8133–8142, doi:10.1002/2016gl070548.
- 1087 Uchida, T., D. Balwada, R. Abernathey, G. McKinley, S. Smith, and M. Lévy, 2019: The Contribu-  
1088 tion of Submesoscale over Mesoscale Eddy Iron Transport in the Open Southern Ocean *Journal*  
1089 *of Advances in Modeling Earth Systems*, **11** (12), 3934–3958, doi:10.1029/2019MS001805.
- 1090 Viúdez, A., 2018: Two modes of vertical velocity in subsurface mesoscale eddies. *Journal of*  
1091 *Geophysical Research: Oceans*, **123** (5), 3705–3722, doi:10.1029/2017JC013735.
- 1092 Viúdez, Á., and D. G. Dritschel, 2004: Potential Vorticity and the Quasigeostrophic and Semi-  
1093 geostrophic Mesoscale Vertical Velocity. *Journal of Physical Oceanography*, **34** (4), 865–887,  
1094 doi:10.1175/1520-0485(2004)034<0865:pvatqa>2.0.co;2.
- 1095 Viúdez, Á., J. Tintoré, and R. L. Haney, 2002: About the Nature of the Generalized Omega  
1096 Equation. *Journal of the Atmospheric Sciences*, **53** (5), 787–795, doi:10.1175/1520-0469(1996)  
1097 053<0787:atnotg>2.0.co;2.

- 1098 Volkov, D. L., and L.-L. Fu, 2010: On the Reasons for the Formation and Variability of the Azores  
1099 Current. *Journal of Physical Oceanography*, **40** (10), 2197–2220, doi:10.1175/2010jpo4326.1.
- 1100 Volkov, D. L., and L. L. Fu, 2011: Interannual variability of the Azores Current strength and eddy  
1101 energy in relation to atmospheric forcing. *Journal of Geophysical Research: Oceans*, **116** (11),  
1102 doi:10.1029/2011JC007271.
- 1103 Whitt, D. B., M. Lévy, and J. R. Taylor, 2019: Submesoscales enhance storm-driven vertical mix-  
1104 ing of nutrients : insights from a biogeochemical large eddy simulation. *Journal of Geophysical*  
1105 *Research*, doi:10.1029/.
- 1106 Whitt, D. B., and L. N. Thomas, 2013: Near-Inertial Waves in Strongly Baroclinic Currents.  
1107 *Journal of Physical Oceanography*, **43** (4), 706–725, doi:10.1175/jpo-d-12-0132.1.
- 1108 Xie, L., E. Pallàs-Sanz, Q. Zheng, S. Zhang, X. Zong, X. Yi, and M. Li, 2017: Diagnosis of 3D  
1109 vertical circulation in the upwelling and frontal zones east of Hainan Island, China. *Journal of*  
1110 *Physical Oceanography*, **47** (4), 755–774, doi:10.1175/JPO-D-16-0192.1.
- 1111 Yoshikawa, Y., C. M. Lee, and L. N. Thomas, 2012: The Subpolar Front of the Japan/East Sea. Part  
1112 III: Competing Roles of Frontal Dynamics and Atmospheric Forcing in Driving Ageostrophic  
1113 Vertical Circulation and Subduction. *Journal of Physical Oceanography*, **42** (6), 991–1011, doi:  
1114 10.1175/jpo-d-11-0154.1.
- 1115 Yu, X., A. C. Naveira Garabato, A. P. Martin, C. E. Buckingham, L. Brannigan, and Z. Su, 2019:  
1116 An annual cycle of submesoscale vertical flow and restratification in the upper ocean. *Journal*  
1117 *of Physical Oceanography*, **49**, 1439–1461, doi:10.1175/JPO-D-18-0253.1.

1118 **LIST OF TABLES**

1119 **Table 1.** Statistics derived from the spectral coherence field (fig.8). Note that relating  
 1120 the horizontal scale  $L_{0.6}$  to the deformation radius,  $R_d$ , which is  $\sim 15$  km in the  
 1121 OSM and REK regions and  $\sim 30$  km in the LMX and AZO regions, yields a  
 1122 performance threshold of  $0.3R_d$  on average, with a minimum  $0.17R_d$  in winter  
 1123 OSM and a maximum  $0.49R_d$  in winter REK. In the AZO region in December  
 1124 the squared coherence never exceeds 0.6 thus leading to a fraction of variance  
 1125 null. . . . . 55

1126 **Table 2.** Averaged errors (in  $\text{m day}^{-1}$  and percentage of  $w_{model}$ ), at depths  $z_a$ , for  $\omega$   
 1127 with perfect right hand side ( $\omega_{\dagger}$ ), perfect boundaries ( $\omega_{NG}^*$ ) and both ( $\omega_{\dagger}^*$ ). See  
 1128 section 2b for the detail on the computation of  $\omega$ . . . . . 56

1129 TABLE 1. Statistics derived from the spectral coherence field (fig.8). Note that relating the horizontal scale  
 1130  $L_{0.6}$  to the deformation radius,  $R_d$ , which is  $\sim 15$  km in the OSM and REK regions and  $\sim 30$  km in the LMX  
 1131 and AZO regions, yields a performance threshold of  $0.3R_d$  on average, with a minimum  $0.17R_d$  in winter OSM  
 1132 and a maximum  $0.49R_d$  in winter REK. In the AZO region in December the squared coherence never exceeds  
 1133 0.6 thus leading to a fraction of variance null.

	Horizontal scale $L_{0.6}$ [km] (and wavelength [km]) below which the squared coherence between true and reconstructed vertical velocities is below 0.6. Values are provided for QG and NG reconstructions				fraction of vertical velocity variance retained by the reconstructed vertical velocity over the scale range $L > L_{0.6}$ . Values are only provided for the NG reconstruction	
	Jun		Dec		Jun	Dec
	QG	NG	QG	NG		
LMX	9.2 (58)	6.7 (42)	9.5 (60)	7.8 (49)	0.90	0.84
AZO	6.4 (40)	6.3 (40)	-	-	0.74	0
REK	4.7 (30)	4.6 (29)	7.3 (46)	6.5 (41)	0.87	0.61
OSM	3.9 (25)	3.9 (25)	3.0 (19)	2.6 (16)	0.72	0.88



1134 TABLE 2. Averaged errors (in  $\text{m day}^{-1}$  and percentage of  $w_{model}$ ), at depths  $z_a$ , for  $\omega$  with perfect right hand  
 1135 side ( $\omega_{\dagger}$ ), perfect boundaries ( $\omega_{NG}^*$ ) and both ( $\omega_{\dagger}^*$ ). See section 2b for the detail on the computation of  $\omega$ .

	$\omega_{\dagger}^*$		$\omega_{\dagger}$		$\omega_{NG}^*$	
LMX	Jun	Dec	Jun	Dec	Jun	Dec
	0.41 (3%)	0.54 (5%)	4.08 (28%)	2.85 (24%)	4.87 (34%)	5.21 (44%)
AZO	Jun	Dec	Jun	Dec	Jun	Dec
	0.04 (3%)	0.04 (3%)	0.25 (20%)	0.27 (23%)	0.80 (65%)	0.95 (79%)
REK	Jun	Dec	Jun	Dec	Jun	Dec
	0.13 (4%)	0.11 (3%)	0.96 (29%)	1.19 (29%)	1.47 (45%)	2.85 (69%)
OSM	Jun	Dec	Jun	Dec	Jun	Dec
	0.06 (2%)	0.20 (4%)	0.66 (19%)	0.90 (16 %)	2.06 (58%)	2.96 (52 %)

1136 **LIST OF FIGURES**

1137 **Fig. 1.** Model vertical velocity on 10 June 2008 (left) and 10 December 2008 (right) in the a) LMX  
 1138 region, b) AZO region, c) REK region and d) OSM region. The upper horizontal plan  
 1139 corresponds to the depth of analysis ( $z_a = 220$  m in LMX, 250 m in AZO, and 380 m in  
 1140 REK and OSM) . . . . . 59

1141 **Fig. 2.** Vertical velocity in the LMX region on 10 June 2008 (left, a, c, e) and 10 December 2008  
 1142 (right, b, d, f) for the QG inversion (a, b), NG inversion (c, d) and model data (e, f). The thin  
 1143 white (resp. black) lines represent the isopycnals (resp. horizontal velocity,  $m\ s^{-1}$ ). The bold  
 1144 solid (resp. dashed) black line indicates mixed layer base (resp. the analysis depth  $z_a$ ). . . . . 60

1145 **Fig. 3.** As in Fig. 2 but for the AZO region. . . . . 61

1146 **Fig. 4.** As in Fig. 2 but for the REK region. . . . . 62

1147 **Fig. 5.** As in Fig. 2 but for the OSM region. . . . . 63

1148 **Fig. 6.** a,b) Vertical velocity variance power spectra for  $w_{model}$  (solid) and  $\omega_{NG}$  (dashed) at depths  
 1149  $z_a$  in the LMX (black,  $z_a = 220$  m), AZO (green,  $z_a = 250$  m), REK (red,  $z_a = 380$  m), and  
 1150 OSM (blue,  $z_a = 380$  m) regions in a) June and b) December. c,d) Same as (a,b) but for  
 1151  $w_{model}$  (solid) and  $\omega_{NG}^*$  (dashed, the reconstructed  $\omega_{NG}^*$  is computed using perfect boundary  
 1152 conditions). Straight (resp. dashed and dot-dashed) lines indicate  $-2$  (resp.  $-5/3$  and  $-3$ )  
 1153 roll-offs. The bottom (resp. top) horizontal axis displays the length scale (resp. wavelength). . . . . 64

1154 **Fig. 7.** Averaged vertical profiles of (a,b) buoyancy frequency, (c,d) eddy kinetic energy and (e,f)  
 1155 vertical velocity root mean square for the LMX (black), AZO (green), REK (red) and OSM  
 1156 (blue) regions in June (upper panel) and December (lower panel). Note the subpanels with  
 1157 a change of scale to accommodate the large differences in EKE between LMX and the other  
 1158 regions. . . . . 65

1159 **Fig. 8.** a,b) Spectral coherence as a function of scale between  $w_{model}$  and  $\omega_{NG}$  (resp.  $\omega_{QG}$ ) at depths  
 1160  $z_a$  is represented by a solid (resp. dashed) line in the LMX (black), AZO (green), REK (red),  
 1161 and OSM (blue) regions in a) June and b) December. c,d) Same as (a,b) but the dashed line  
 1162 represent the coherence between  $w_{model}$  and  $\omega_{NG}^*$  (the reconstructed  $\omega_{NG}^*$  is computed using  
 1163 perfect boundary conditions). The bottom (resp. top) horizontal axis displays the length  
 1164 scale (resp. wavelength). . . . . 66

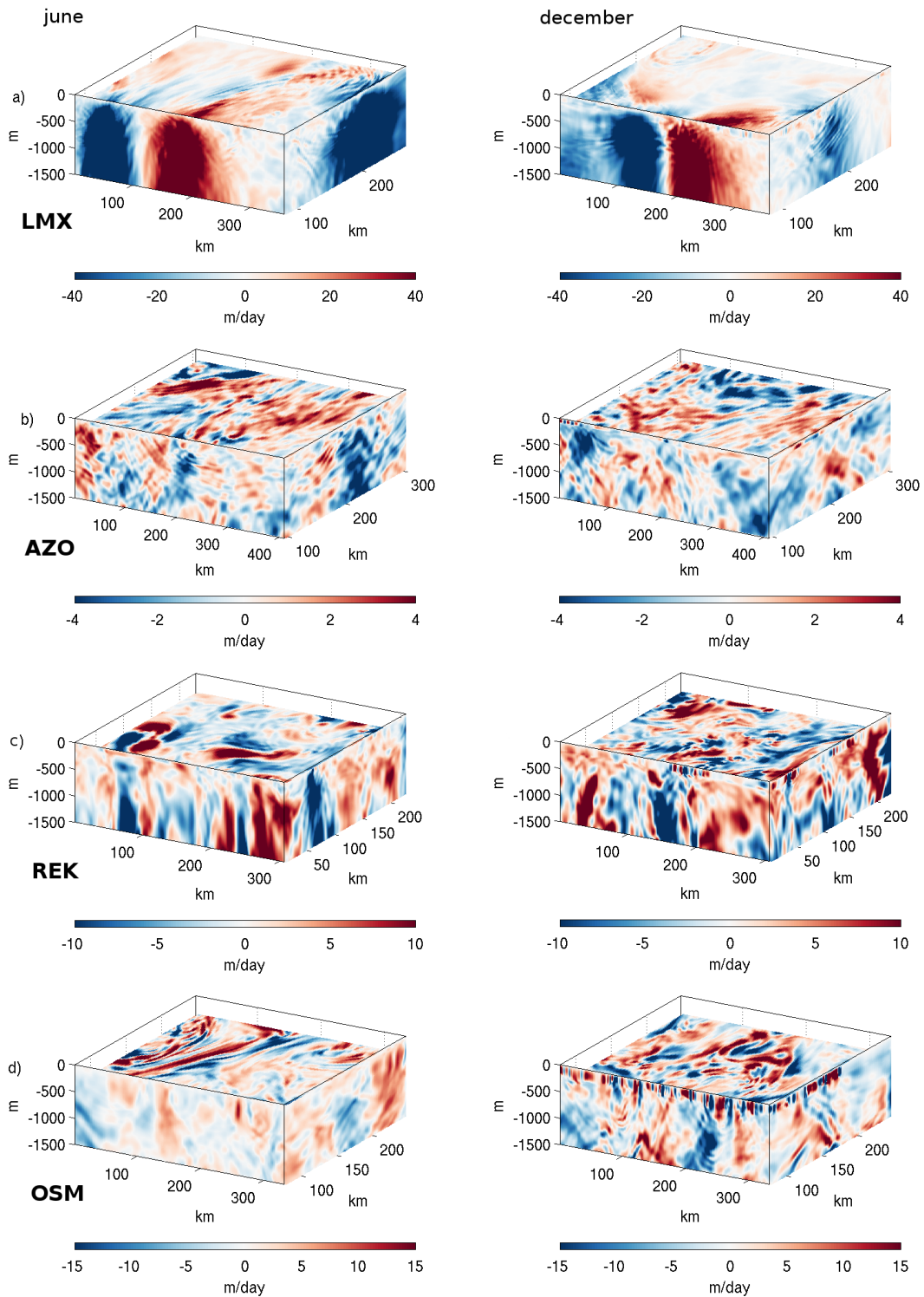
1165 **Fig. 9.** Spectral coherence between  $w_{model}$  and  $\omega_{NG}$  at depths  $z_a$  averaged over the scale ranges (a,  
 1166 b) 10 – 25 km and (c, d) 3 – 10 km as a function of the fraction of variance retained by each  
 1167 averaging intervals. Results are shown for the LMX (black), AZO (green), REK (red), and  
 1168 OSM (blue) regions in June (left, a, c) and December (right, b, d). The markers represent  
 1169 the timespan of the averages: the star is 1 day, square 2 days, diamond 5 days and triangle  
 1170 10 days. The highest coherence is indicated by a larger marker with a black contour. The  
 1171 black dashed lines mark a fraction of variance of 75% and a coherence of 0.6. . . . . 67

1172 **Fig. 10.** Relative error, at depths  $z_a$ , between  $w_{model}$  and  $\omega_{\dagger}$  in June (a-d) and December (e-h) in the  
 1173 LMX (a, e), AZO (b, f), REK (c, g) and OSM (d, h) regions as a function of the depth where  
 1174 the bottom boundary condition ( $z_{bottom}$  in the text) is imposed. Errors for a Dirichlet (resp.  
 1175 Neumann) BBC are represented with a black (resp. blue) line. Black diamonds indicate  
 1176 error values for a Dirichlet boundary condition modified as in Rudnick (1996) (see section  
 1177 4d for details). The vertical bars show the standard deviation over the 11 daily averages used  
 1178 for our analysis. . . . . 68

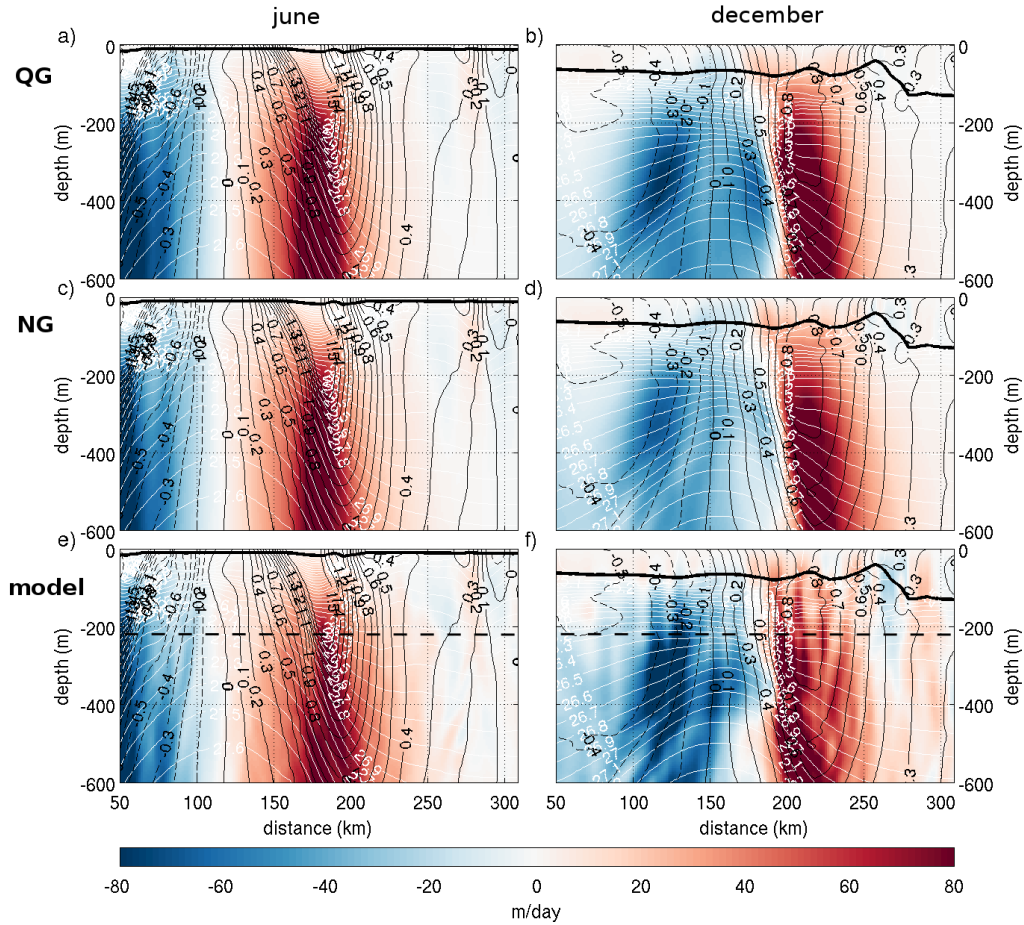
1179 **Fig. 11.** First three baroclinic pressure modes for the a) LMX, b) AZO, c) REK, and d) OSM region  
 1180 in June (red) and December (blue). First three vertical velocity modes for the e) LMX,  
 1181 f) AZO, g) REK, and h) OSM region in June (red) and December (blue). The first mode  
 1182 (resp. 2nd and 3rd modes) is represented with a solid (resp. dashed and dotted) line. The  
 1183 amplitudes of the modes have been scaled so as to vary between  $-1$  and  $1$ . . . . . 69

1184 **Fig. 12.** Percentage of vertical water profiles for which the projection of model  $w$  on the subset of  
 1185 the gravest vertical modes (1, 2 or 3 gravest modes) leads to an approximation of  $w$  with a  
 1186 relative error that is less than 50 %, i.e., percentage of profiles where  $\varepsilon/w < 0.5$  ( $\varepsilon$  being  
 1187 defined in equation A8). Percentages are represented for LMX (black), AZO (green), REK  
 1188 (red) and OSM (blue) in summer (plain lines) and winter (dashed lines). . . . . 70

1189 **Fig. 13.** schematic representation of the vertical disturbance (y-direction) and associated tracer  
 1190 anomaly temporal evolution undergone by a water parcel in 4 different situations. Upper  
 1191 panels: a nutrient-like tracer  $\tau$  with a photosynthesis-like sink term ( $\nabla\tau$  is positive down-  
 1192 ward) in the upper ocean is subjected to a mesoscale (a) and submesoscale (b) vertical oscil-  
 1193 lation (respectively of amplitude  $\delta z^m$  and  $\delta z^s$ ). Lower panels: a tracer with no sink-source  
 1194 term is subjected to a mesoscale (c) and submesoscale (d) vertical oscillation, with a dia-  
 1195 batic redistribution of tracer through shear driven mixing (purple arrows). In all panels, the  
 1196 horizontal direction represent time, increasing from left to tight. Positive (resp., negative  
 1197 and null) tracer concentration anomalies ( $\delta\tau$ ) relative to the parcel depth are represented  
 1198 with green (resp. orange and white) colors. + and - symbols also provide indications on  
 1199 tracer anomalies (resp. positive and negative). In limit case 2, submesoscale oscillation  
 1200 have a lesser impact than mesoscale ones while the opposite may be true in limit case 3 if  
 1201 submesoscale oscillations are more effective to produce shear-driven turbulence. . . . . 71



1202 FIG. 1. Model vertical velocity on 10 June 2008 (left) and 10 December 2008 (right) in the a) LMX region, b)  
 1203 AZO region, c) REK region and d) OSM region. The upper horizontal plan corresponds to the depth of analysis  
 1204 ( $z_a = 220$  m in LMX, 250 m in AZO, and 380 m in REK and OSM)



1205 FIG. 2. Vertical velocity in the LMX region on 10 June 2008 (left, a, c, e) and 10 December 2008 (right, b,  
 1206 d, f) for the QG inversion (a, b), NG inversion (c, d) and model data (e, f). The thin white (resp. black) lines  
 1207 represent the isopycnals (resp. horizontal velocity,  $\text{m s}^{-1}$ ). The bold solid (resp. dashed) black line indicates  
 1208 mixed layer base (resp. the analysis depth  $z_d$ ).

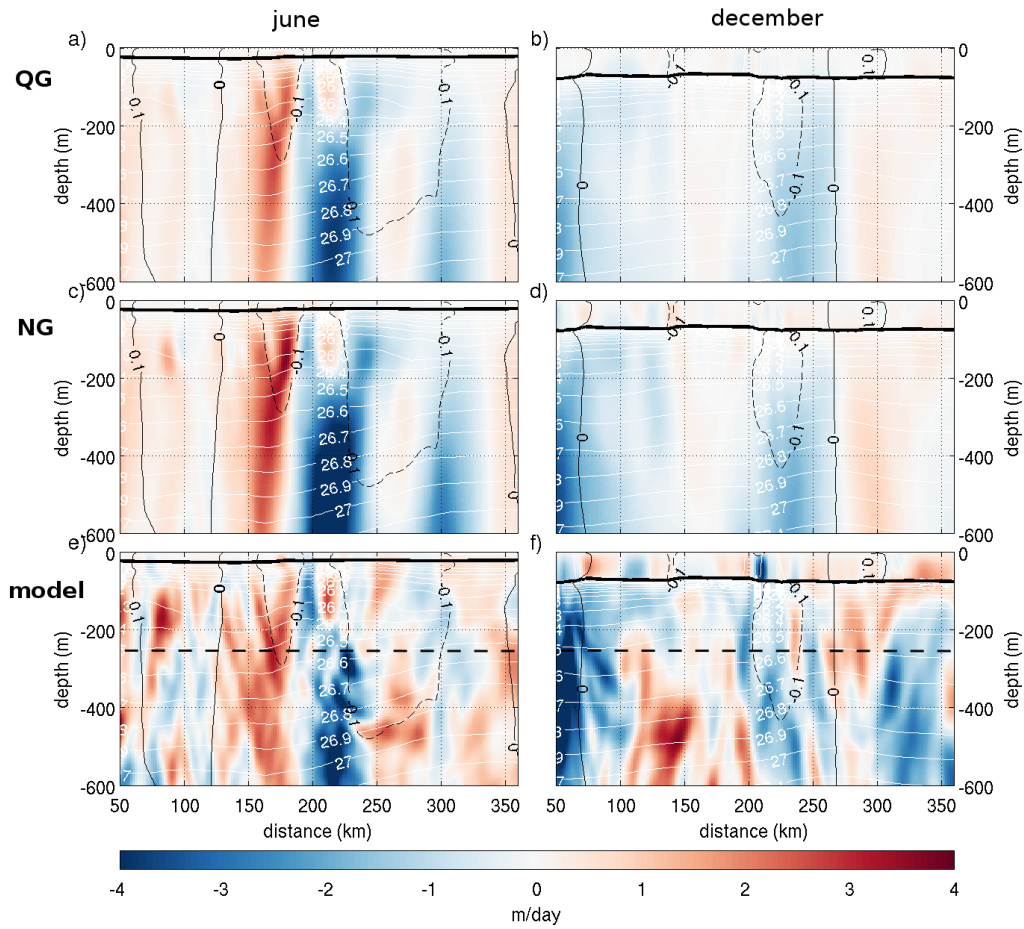


FIG. 3. As in Fig. 2 but for the AZO region.

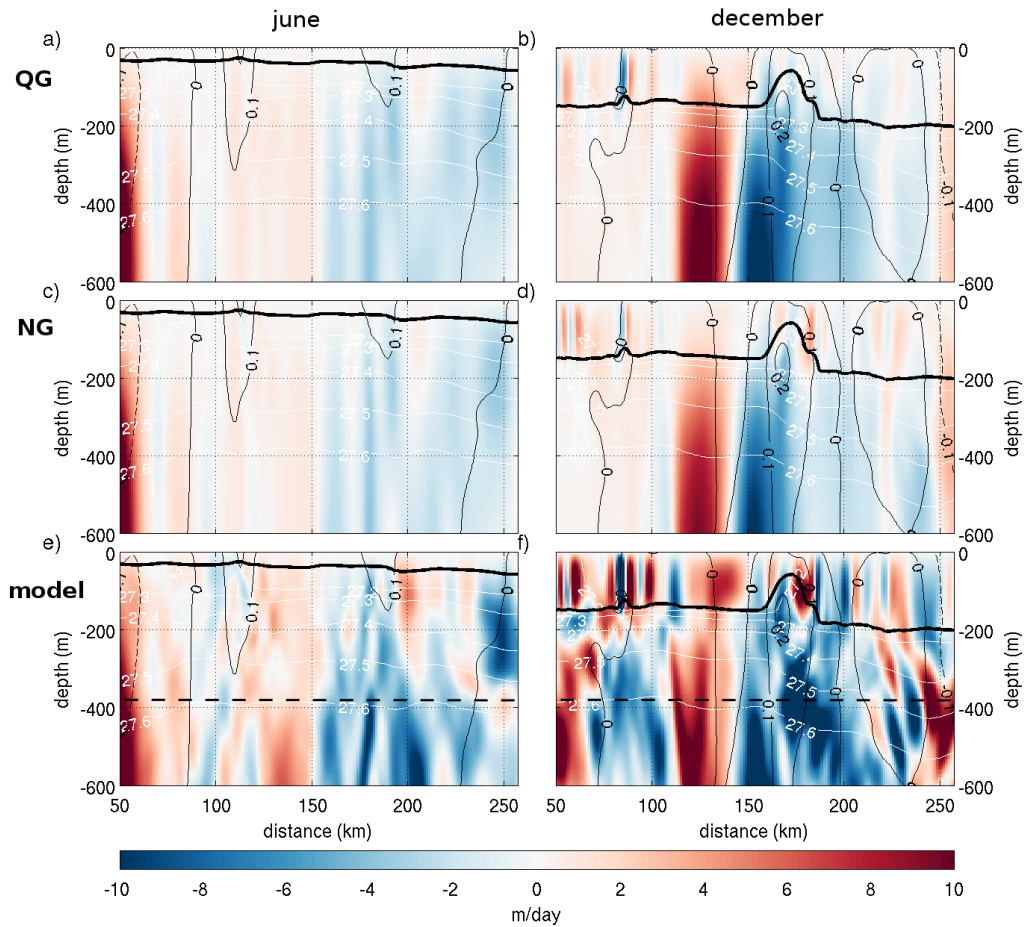


FIG. 4. As in Fig. 2 but for the REK region.

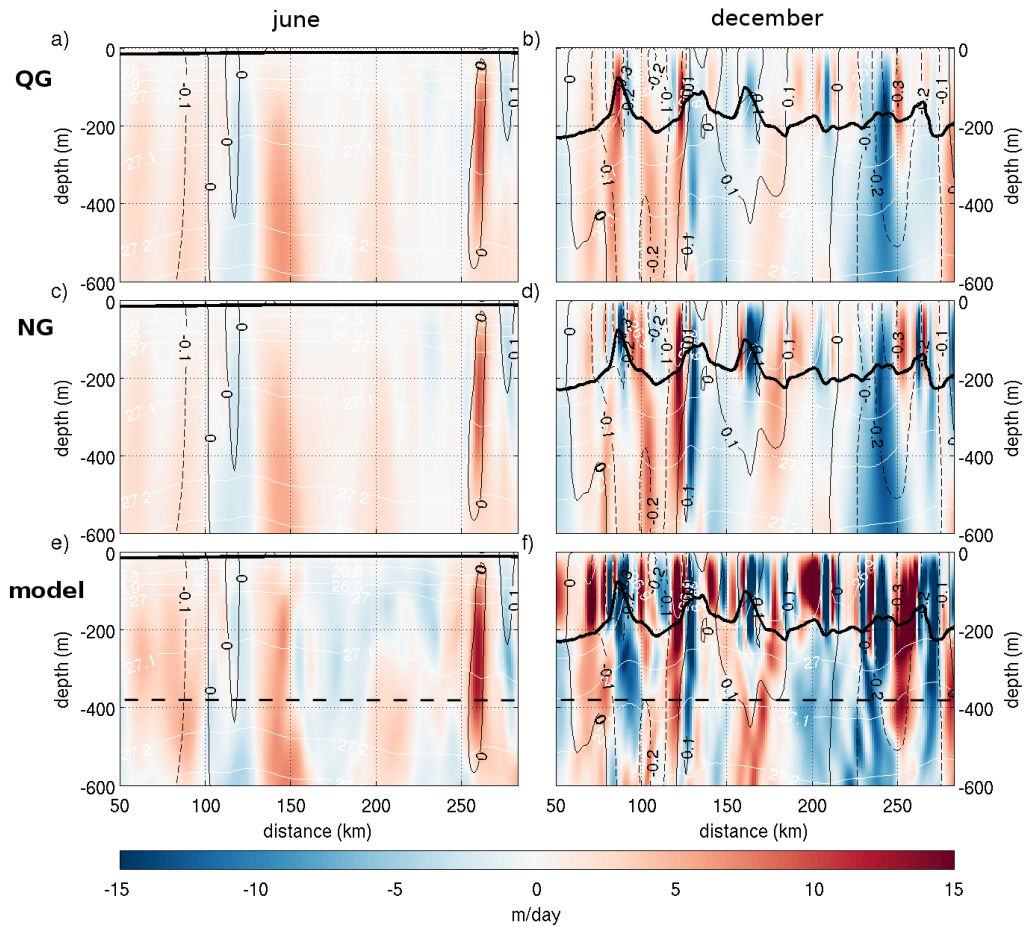
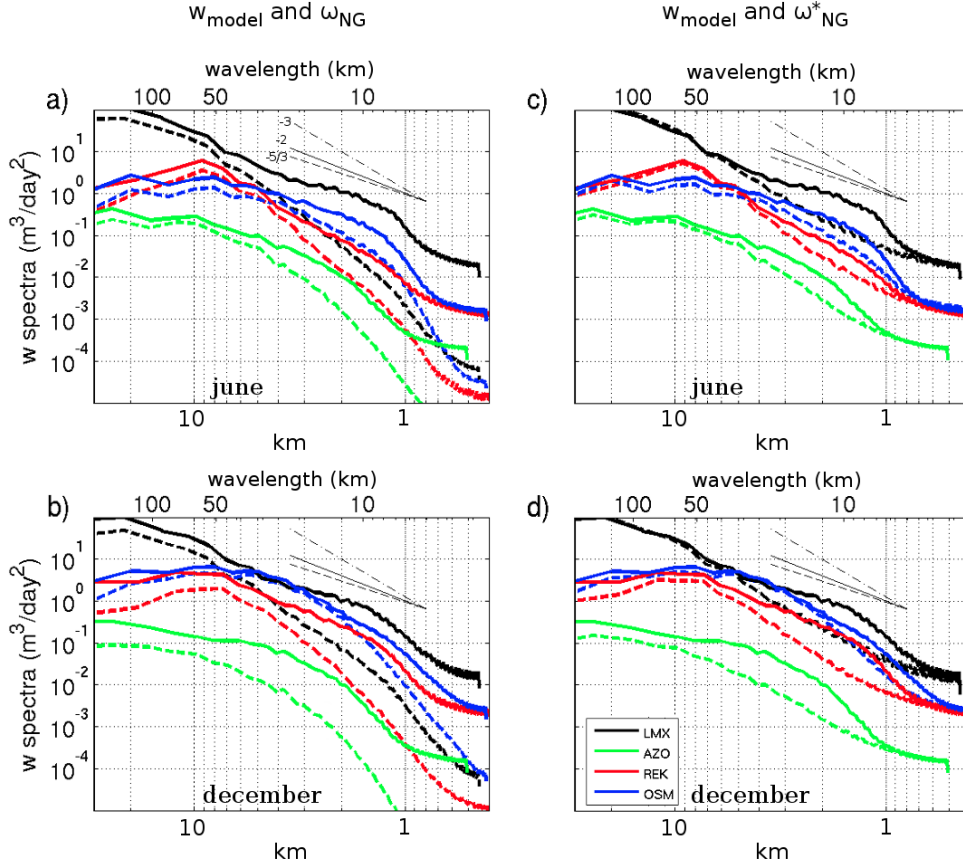
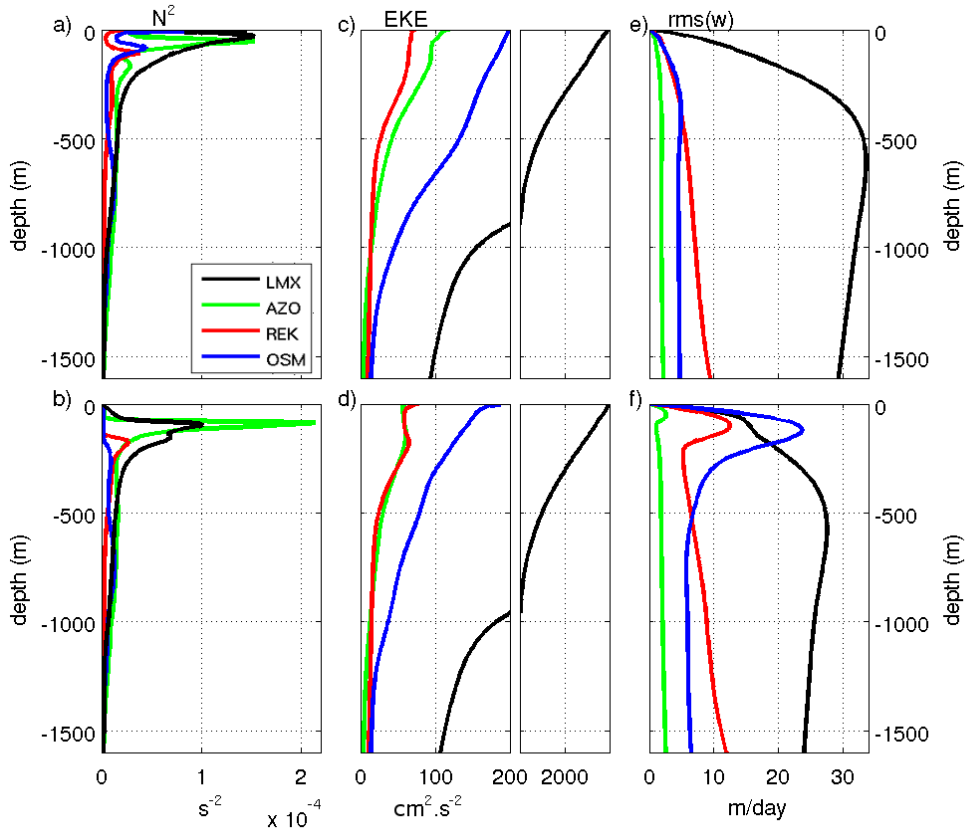


FIG. 5. As in Fig. 2 but for the OSM region.

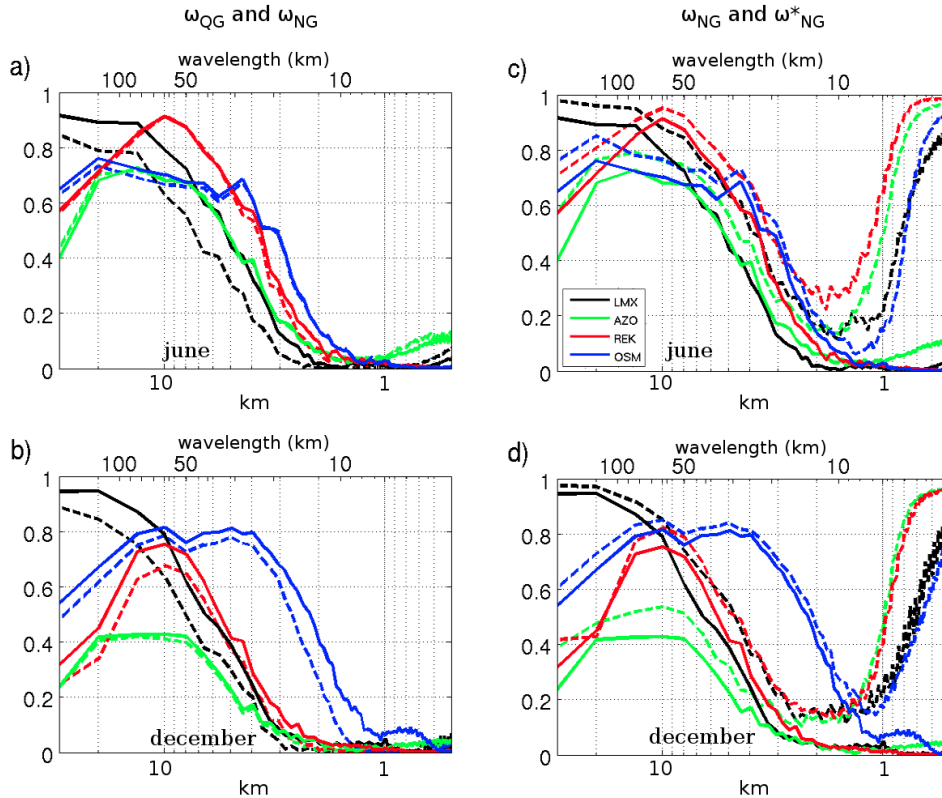




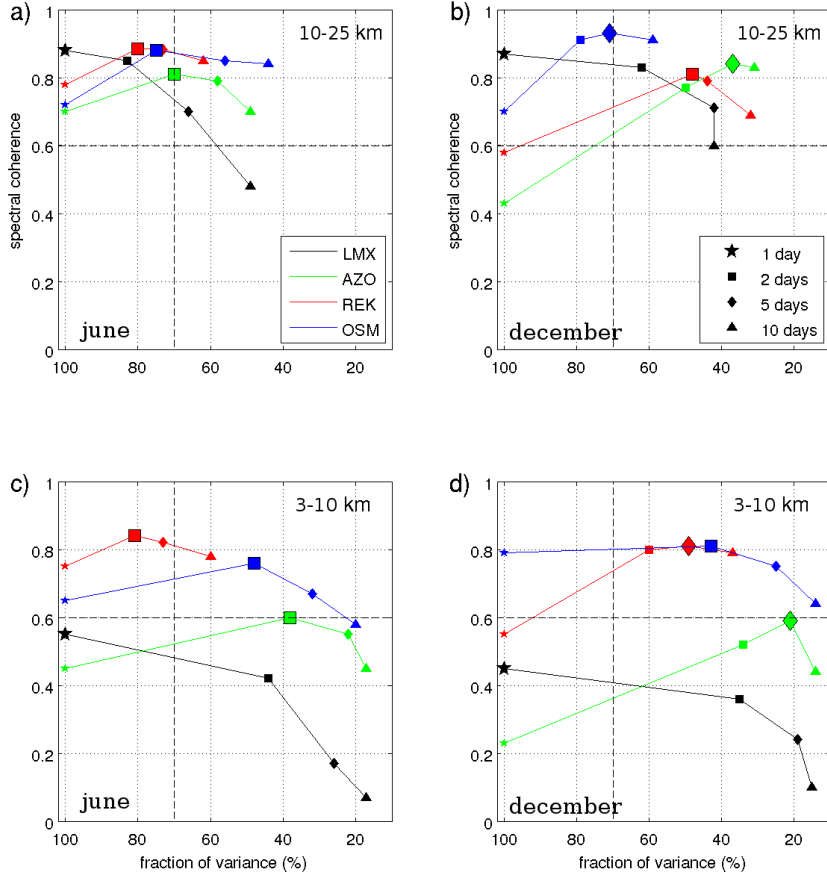
1209 FIG. 6. a,b) Vertical velocity variance power spectra for  $w_{model}$  (solid) and  $\omega_{NG}$  (dashed) at depths  $z_a$  in the  
 1210 LMX (black,  $z_a = 220$  m), AZO (green,  $z_a = 250$  m), REK (red,  $z_a = 380$  m), and OSM (blue,  $z_a = 380$  m)  
 1211 regions in a) June and b) December. c,d) Same as (a,b) but for  $w_{model}$  (solid) and  $\omega_{NG}^*$  (dashed, the reconstructed  
 1212  $\omega_{NG}^*$  is computed using perfect boundary conditions). Straight (resp. dashed and dot-dashed) lines indicate  
 1213  $-2$  (resp.  $-5/3$  and  $-3$ ) roll-offs. The bottom (resp. top) horizontal axis displays the length scale (resp.  
 1214 wavelength).



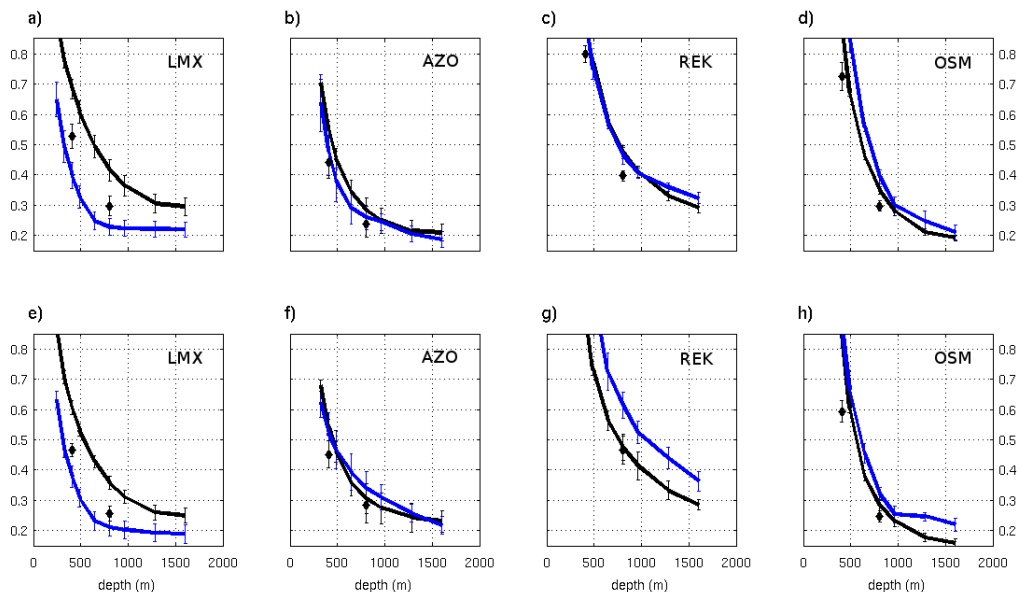
1215 FIG. 7. Averaged vertical profiles of (a,b) buoyancy frequency, (c,d) eddy kinetic energy and (e,f) vertical  
 1216 velocity root mean square for the LMX (black), AZO (green), REK (red) and OSM (blue) regions in June  
 1217 (upper panel) and December (lower panel). Note the subpanels with a change of scale to accommodate the large  
 1218 differences in EKE between LMX and the other regions.



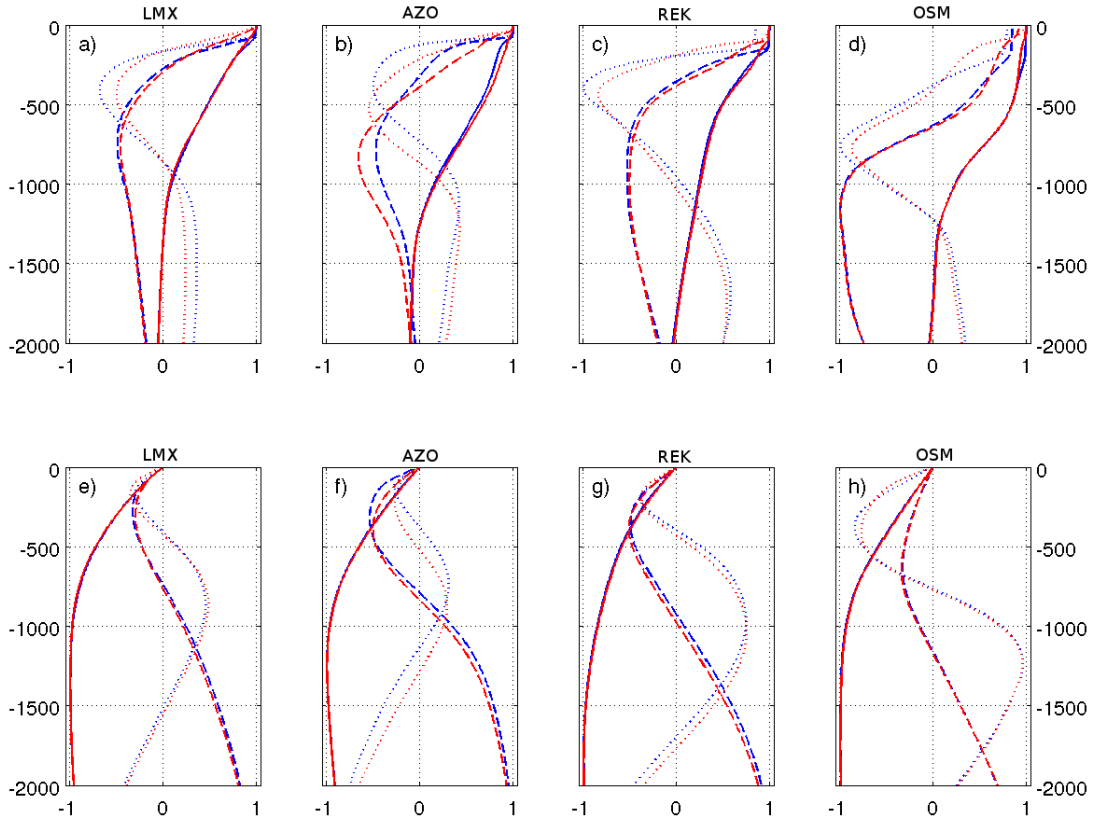
1219 FIG. 8. a,b) Spectral coherence as a function of scale between  $w_{model}$  and  $\omega_{NG}$  (resp.  $\omega_{QG}$ ) at depths  $z_a$  is  
 1220 represented by a solid (resp. dashed) line in the LMX (black), AZO (green), REK (red), and OSM (blue) regions  
 1221 in a) June and b) December. c,d) Same as (a,b) but the dashed line represent the coherence between  $w_{model}$  and  
 1222  $\omega_{NG}^*$  (the reconstructed  $\omega_{NG}^*$  is computed using perfect boundary conditions). The bottom (resp. top) horizontal  
 1223 axis displays the length scale (resp. wavelength).



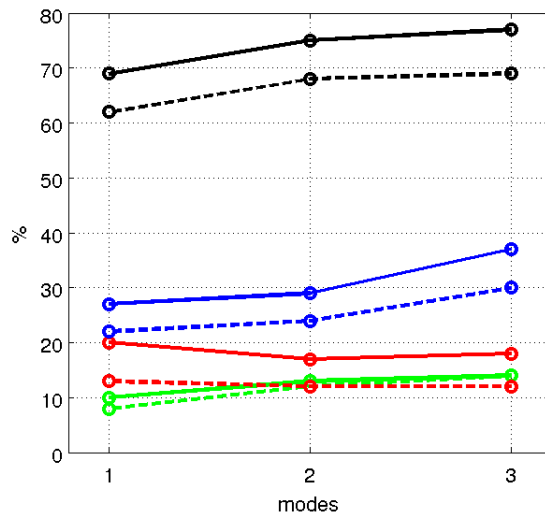
1224 FIG. 9. Spectral coherence between  $w_{model}$  and  $\omega_{NG}$  at depths  $z_a$  averaged over the scale ranges (a, b) 10 – 25  
 1225 km and (c, d) 3 – 10 km as a function of the fraction of variance retained by each averaging intervals. Results are  
 1226 shown for the LMX (black), AZO (green), REK (red), and OSM (blue) regions in June (left, a, c) and December  
 1227 (right, b, d). The markers represent the timespan of the averages: the star is 1 day, square 2 days, diamond 5  
 1228 days and triangle 10 days. The highest coherence is indicated by a larger marker with a black contour. The black  
 1229 dashed lines mark a fraction of variance of 75% and a coherence of 0.6.



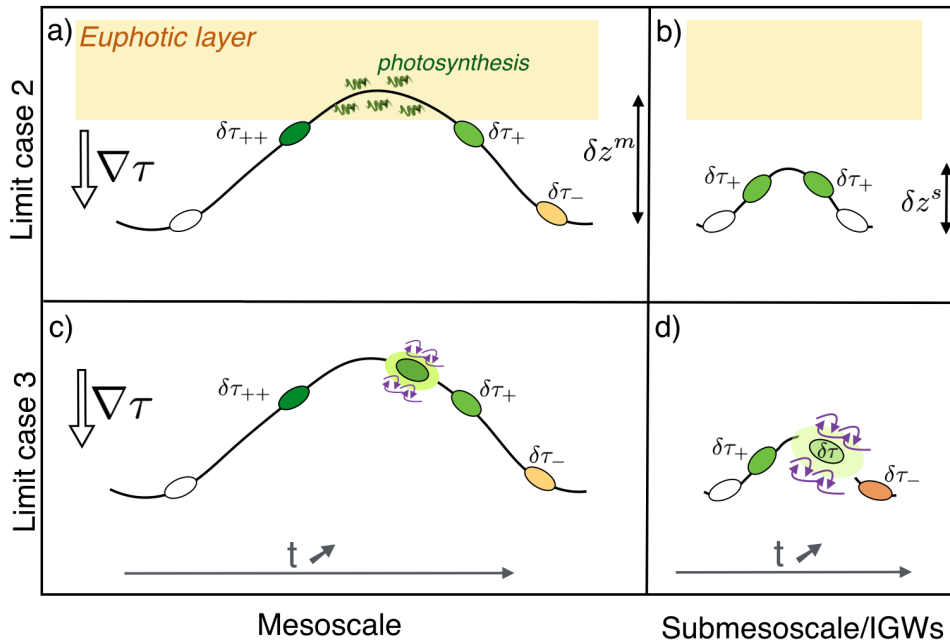
1230 FIG. 10. Relative error, at depths  $z_a$ , between  $w_{model}$  and  $\omega_{\mp}$  in June (a-d) and December (e-h) in the LMX  
 1231 (a, e), AZO (b, f), REK (c, g) and OSM (d, h) regions as a function of the depth where the bottom boundary  
 1232 condition ( $z_{bottom}$  in the text) is imposed. Errors for a Dirichlet (resp. Neumann) BBC are represented with a  
 1233 black (resp. blue) line. Black diamonds indicate error values for a Dirichlet boundary condition modified as  
 1234 in Rudnick (1996) (see section 4d for details). The vertical bars show the standard deviation over the 11 daily  
 1235 averages used for our analysis.



1236 FIG. 11. First three baroclinic pressure modes for the a) LMX, b) AZO, c) REK, and d) OSM region in June  
 1237 (red) and December (blue). First three vertical velocity modes for the e) LMX, f) AZO, g) REK, and h) OSM  
 1238 region in June (red) and December (blue). The first mode (resp. 2nd and 3rd modes) is represented with a solid  
 1239 (resp. dashed and dotted) line. The amplitudes of the modes have been scaled so as to vary between  $-1$  and  $1$ .



1240 FIG. 12. Percentage of vertical water profiles for which the projection of model  $w$  on the subset of the gravest  
 1241 vertical modes (1, 2 or 3 gravest modes) leads to an approximation of  $w$  with a relative error that is less than 50  
 1242 %, i.e., percentage of profiles where  $\varepsilon/w < 0.5$  ( $\varepsilon$  being defined in equation A8). Percentages are represented  
 1243 for LMX (black), AZO (green), REK (red) and OSM (blue) in summer (plain lines) and winter (dashed lines).



1244 FIG. 13. schematic representation of the vertical disturbance (y-direction) and associated tracer anomaly tem-  
 1245 poral evolution undergone by a water parcel in 4 different situations. Upper panels: a nutrient-like tracer  $\tau$  with  
 1246 a photosynthesis-like sink term ( $\nabla\tau$  is positive downward) in the upper ocean is subjected to a mesoscale (a) and  
 1247 submesoscale (b) vertical oscillation (respectively of amplitude  $\delta z^m$  and  $\delta z^s$ ). Lower panels: a tracer with no  
 1248 sink-source term is subjected to a mesoscale (c) and submesoscale (d) vertical oscillation, with a diabatic redis-  
 1249 tribution of tracer through shear driven mixing (purple arrows). In all panels, the horizontal direction represent  
 1250 time, increasing from left to tight. Positive (resp., negative and null) tracer concentration anomalies ( $\delta\tau$ ) relative  
 1251 to the parcel depth are represented with green (resp. orange and white) colors. + and - symbols also provide  
 1252 indications on tracer anomalies (resp. positive and negative). In limit case 2, submesoscale oscillation have a  
 1253 lesser impact than mesoscale ones while the opposite may be true in limit case 3 if submesoscale oscillations are  
 1254 more effective to produce shear-driven turbulence.